

UCLA

UCLA Previously Published Works

Title

A cancer cell-intrinsic GOT2-PPAR δ axis suppresses antitumor immunity

Permalink

<https://escholarship.org/uc/item/3s17d4fn>

Journal

Cancer Discovery, 12(10)

ISSN

2159-8274

Authors

Abrego, Jaime
Sanford-Crane, Hannah
Oon, Chet
[et al.](#)

Publication Date

2022-10-05

DOI

10.1158/2159-8290.cd-22-0661

Peer reviewed

A Cancer Cell-Intrinsic GOT2-PPAR δ Axis Suppresses Antitumor Immunity



Jaime Abrego¹, Hannah Sanford-Crane¹, Chet Oon¹, Xu Xiao², Courtney B. Betts¹, Duanchen Sun³, Shanthi Nagarajan⁴, Luis Diaz¹, Holly Sandborg¹, Sohinee Bhattacharyya¹, Zheng Xia^{3,5}, Lisa M. Coussens^{1,5}, Peter Tontonoz^{2,6}, and Mara H. Sherman^{1,5}



ABSTRACT

Despite significant recent advances in precision medicine, pancreatic ductal adenocarcinoma (PDAC) remains near uniformly lethal. Although immune-modulatory therapies hold promise to meaningfully improve outcomes for patients with PDAC, the development of such therapies requires an improved understanding of the immune evasion mechanisms that characterize the PDAC microenvironment. Here, we show that cancer cell-intrinsic glutamic-oxaloacetic transaminase 2 (GOT2) shapes the immune microenvironment to suppress antitumor immunity. Mechanistically, we find that GOT2 functions beyond its established role in the malate–aspartate shuttle and promotes the transcriptional activity of nuclear receptor peroxisome proliferator-activated receptor delta (PPAR δ), facilitated by direct fatty acid binding. Although GOT2 is dispensable for cancer cell proliferation *in vivo*, the GOT2–PPAR δ axis promotes spatial restriction of both CD4⁺ and CD8⁺ T cells from the tumor microenvironment. Our results demonstrate a noncanonical function for an established mitochondrial enzyme in transcriptional regulation of immune evasion, which may be exploitable to promote a productive antitumor immune response.

SIGNIFICANCE: Prior studies demonstrate the important moonlighting functions of metabolic enzymes in cancer. We find that the mitochondrial transaminase GOT2 binds directly to fatty acid ligands that regulate the nuclear receptor PPAR δ , and this functional interaction critically regulates the immune microenvironment of pancreatic cancer to promote tumor progression.

See related commentary by Nwosu and di Magliano, p. 2237.

INTRODUCTION

Dual functions for glutamic-oxaloacetic transaminase 2 (GOT2) are described in the literature. The far better studied function is as a mitochondrial transaminase, implicated in the maintenance of the malate–aspartate shuttle and redox homeostasis (1–4). However, a limited body of evidence indicates a role for GOT2 in fatty acid binding and trafficking (5–10), though this role remains poorly understood and has not been investigated in cancer. In these studies, GOT2 is often referred to as plasma membrane fatty acid binding protein (FABPpm) due to its membrane-proximal localization in hepatocytes and the ability of GOT2/FABPpm antiserum to disrupt fatty acid trafficking in metabolic cell types, including hepatocytes and cardiomyocytes (5, 11–13). In light of recent work from our group and others documenting the importance of fatty acid

trafficking for solid tumor progression (14–18), we considered that GOT2 may promote pancreatic ductal adenocarcinoma (PDAC) growth, at least in part through its fatty acid trafficking function. GOT2 is overexpressed in human PDAC (19), and although transmembrane fatty acid transporters were variably expressed, GOT2 was consistently expressed in human PDAC per two independent RNA sequencing (RNA-seq) data sets (Supplementary Fig. S1A and S1B), as was the cytosolic isoform GOT1. We set out to determine whether GOT2 plays a role in PDAC progression *in vivo* and, if so, to understand the relevance of its established mitochondrial role versus its less characterized role in spatial regulation of fatty acids.

RESULTS

To assess the significance of GOT2 for PDAC progression, we generated several loss-of-function systems using short hairpin RNA (shRNA) or CRISPR/Cas9 and using human and murine PDAC cells (Supplementary Fig. S2A). Cas9 and single-guide RNAs (sgRNA) were introduced by transient transfection, and Cas9 was no longer expressed by the time cells were used for *in vivo* studies; GOT1 levels were unchanged (Supplementary Fig. S2B). Across all cell lines tested, only two showed proliferation defects (Fig. 1A; Supplementary Fig. S2C). These defects were modest, and, in one of the two lines, a reduction in proliferation was seen only upon inducible GOT2 knockdown, suggesting that PDAC cells have sufficient metabolic plasticity to adapt to GOT2 loss and maintain proliferative capacity. However, when sgGot2 PDAC cells were transplanted into pancreata of immune-competent syngeneic hosts, tumor growth was severely compromised (Fig. 1B). Consistent with *in vitro* results, proliferation among tumor cells was not impaired *in vivo* (Fig. 1C). An independent model also revealed a critical role for GOT2 in PDAC growth, whether GOT2 was knocked down with shRNA (Fig. 1D) or knocked out with CRISPR/Cas9 (Fig. 1E; Supplementary Fig. S2D). Though shRNA-mediated knockdown had a less dramatic effect on tumor growth, we

¹Department of Cell, Developmental and Cancer Biology, Oregon Health & Science University, Portland, Oregon. ²Department of Pathology and Laboratory Medicine, David Geffen School of Medicine, University of California, Los Angeles, Los Angeles, California. ³Computational Biology Program, Oregon Health & Science University, Portland, Oregon. ⁴Medicinal Chemistry Core, Oregon Health & Science University, Portland, Oregon. ⁵Knight Cancer Institute, Oregon Health & Science University, Portland, Oregon. ⁶Department of Biological Chemistry, University of California, Los Angeles, Los Angeles, California.

Note: J. Abrego and H. Sanford-Crane contributed equally to this article. Current address for S. Nagarajan: Discovery Chemistry and Research Technologies, Lilly Research Laboratories, Eli Lilly and Company, Lilly Corporate Center, Indianapolis, Indiana.

Corresponding Author: Mara H. Sherman, Department of Cell, Developmental and Cancer Biology, Oregon Health and Science University, 2730 South Moody Avenue CL6C, Portland, OR 97201. Phone: 503-346-9012; E-mail: shermama@ohsu.edu

Cancer Discov 2022;12:2414–33

doi: 10.1158/2159-8290.CD-22-0661

This open access article is distributed under the Creative Commons Attribution-NonCommercial-NoDerivatives 4.0 International (CC BY-NC-ND 4.0) license.

©2022 The Authors; Published by the American Association for Cancer Research

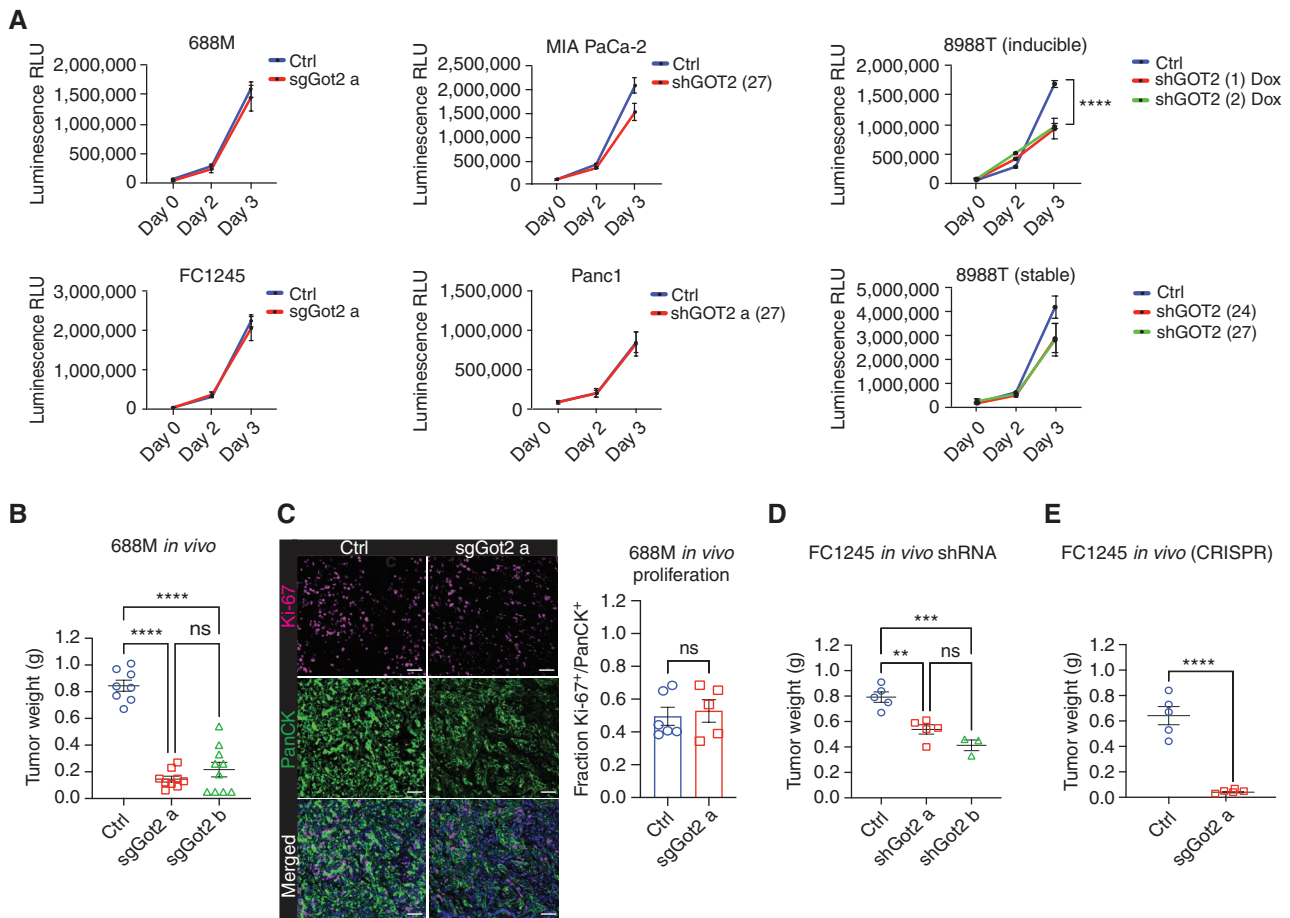
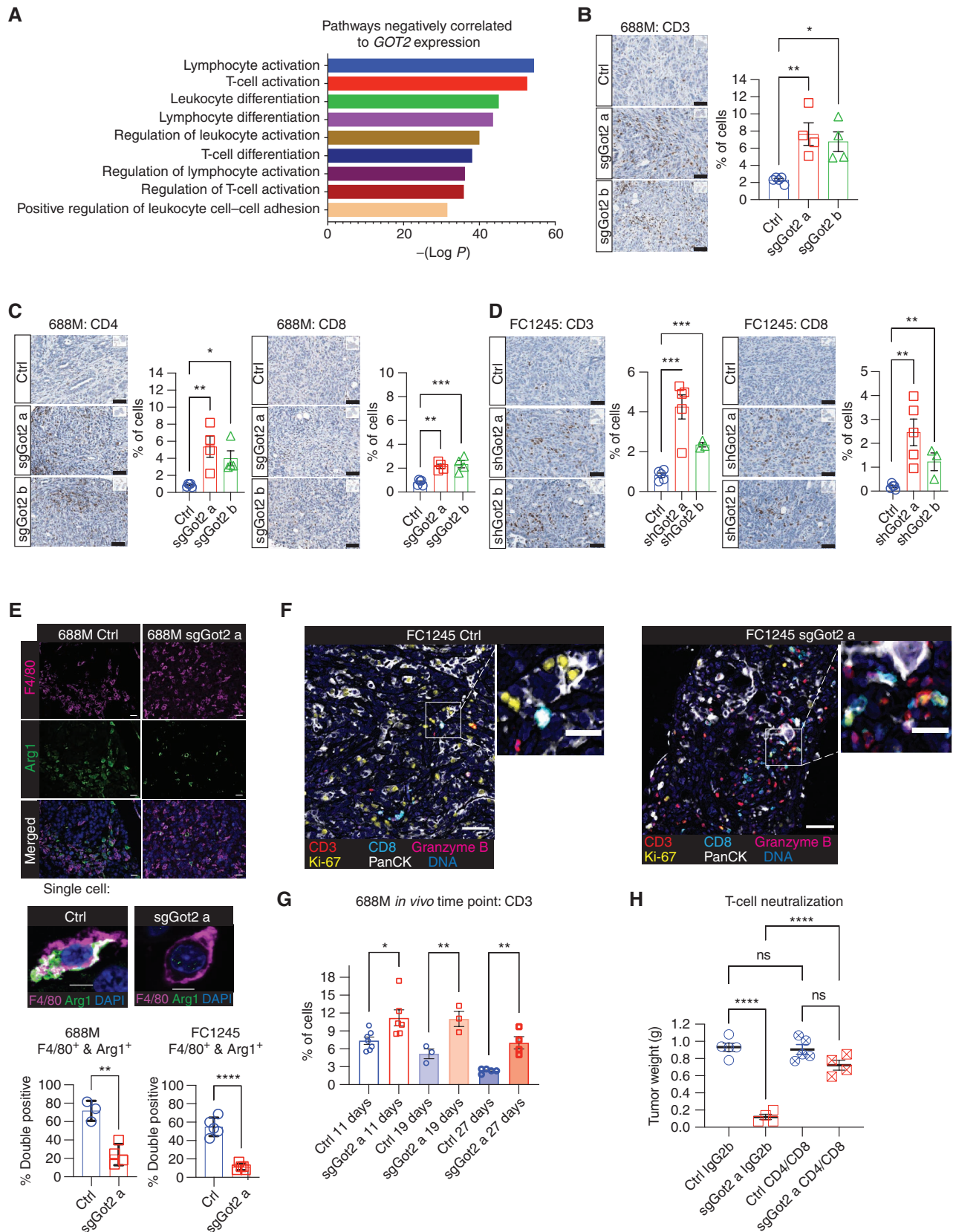


Figure 1. GOT2 promotes pancreatic tumor progression without impacting proliferation. **A**, Viable cell measurements in the indicated PDAC cell lines. Data are presented as mean \pm SEM from biological triplicates. ****, $P < 0.0001$ by one-way ANOVA. Dox, doxycycline; RLU, relative light unit. Numbers in parentheses are the short hairpins (shRNAs) used for the GOT2 knockdowns. **B**, PDAC tumor weight at the experimental endpoint, 34 days after orthotopic transplantation of 688M cells into immune-competent hosts. Ctrl: $n = 8$, sgGot2 a: $n = 9$, sgGot2 b: $n = 10$. Data are presented as mean \pm SEM. ns = not significant. ****, $P < 0.0001$ by one-way ANOVA. **C**, IHC staining of tumors in **B** for Ki-67 (proliferation) and pan-cytokeratin (panCK; tumor cells), with a DAPI counterstain (nuclei). Representative images are shown on the left (scale bars = 50 μ m), with quantification on the right (ctrl: $n = 6$, sgGot2: $n = 5$). Data are presented as mean \pm SEM. ns = not significant by an unpaired t test. **D**, PDAC tumor weight at the experimental endpoint, 22 days after orthotopic transplantation of FC1245 cells into immune-competent hosts. Ctrl: $n = 5$, shGot2 a: $n = 5$, shGot2 b: $n = 3$. Data are presented as mean \pm SEM. ns = not significant. **, $P < 0.01$; ****, $P < 0.0001$ by one-way ANOVA. **E**, PDAC tumor weight at the experimental endpoint, 18 days after orthotopic transplantation of FC1245 cells into immune-competent hosts. Ctrl: $n = 5$, sgGot2 a: $n = 5$. Data are presented as mean \pm SEM. ****, $P < 0.0001$ by an unpaired t test.

noted a partial recovery of GOT2 expression in these tumors by the experimental endpoint (Supplementary Fig. S2E). These results indicated that GOT2 is dispensable for PDAC cell proliferation but required for tumor growth *in vivo* and raised the possibility that cancer cell-intrinsic GOT2 promotes growth-permissive regulation of the tumor microenvironment.

To gain insight into GOT2 function in an intact tumor microenvironment, we identified transcriptional programs with expression inversely correlated with GOT2 transcript abundance in The Cancer Genome Atlas (TCGA) RNA-seq data (Fig. 2A). Pathway analysis of this group of genes revealed enrichment for genes associated with lymphocyte

Figure 2. PDAC cell-intrinsic GOT2 suppresses T cell-dependent immunologic control of tumor growth. **A**, Metascape pathway analysis depicting the top transcriptional programs inversely correlated with GOT2 expression in human PDAC. **B** and **C**, IHC staining of control and sgGot2 688M tumors for T-cell marker CD3 (**B**) and subtype markers CD4 and CD8 (**C**). Representative images are shown on the left (scale bars = 50 μ m), with quantification on the right (ctrl: $n = 5$, sgGot2 a: $n = 4$, sgGot2 b: $n = 4$). Data are presented as mean \pm SEM. *, $P < 0.05$; **, $P < 0.01$; ****, $P < 0.0001$ by one-way ANOVA. **D**, IHC staining of control and shGot2 FC1245 tumors for T-cell markers CD3 and CD8. Representative images are shown on the left (scale bars = 50 μ m), with quantification on the right (ctrl: $n = 5$, shGot2 a: $n = 5$, shGot2 b: $n = 3$). Data are presented as mean \pm SEM. **, $P < 0.01$; ****, $P < 0.0001$ by one-way ANOVA. **E**, IHC costaining of control and sgGot2 or shGot2 PDAC for macrophage marker F4/80 and immunosuppressive factor arginase-1 (Arg1). Representative images are from 688M tumors (scale bar on 20 \times images = 10 μ m, scale bar on 63 \times images = 5 μ m). Quantification of double-positive cells out of total F4/80 $^{+}$ cells in the 688M and FC1245 models is on the right; data are presented as mean \pm SEM. **, $P < 0.01$; ****, $P < 0.0001$ by an unpaired t test. **F**, Multiplex IHC staining of control and sgGot2 FC1245 tumors for the indicated markers (large images, scale bar = 50 μ m; insets, scale bar = 20 μ m). **G**, Quantification of CD3 IHC on 688M PDAC at the indicated time points after transplantation (ctrl d11: $n = 7$, sgGot2 a d11: $n = 6$, ctrl d19: $n = 3$, sgGot2 a d19: $n = 3$, ctrl d27: $n = 5$, sgGot2 a d27: $n = 4$). *, $P < 0.05$; **, $P < 0.01$ by an unpaired t test. **H**, PDAC tumor weight at the experimental endpoint, 27 days after orthotopic transplantation of 688M cells and treatment with isotype control or T-cell depleting antibodies (details in Methods). Ctrl: $n = 5$ per cohort, sgGot2 a: $n = 4$ per cohort. Data are presented as mean \pm SEM. ns = not significant. ****, $P < 0.0001$ by one-way ANOVA.



differentiation, activation, and adhesion and led us to question whether cancer cell-intrinsic GOT2 regulates the abundance and/or activity of intratumoral T cells. Transcripts positively correlated with *GOT2* were involved in metabolic processes (Supplementary Fig. S2F). We quantified T cells in two independent GOT2 loss-of-function models and found that T-cell frequencies were increased in sgGot2 or shGot2 tumors compared with controls, including CD4⁺ and CD8⁺ T cells (Fig. 2B–D). As PDAC contains high numbers of immune-suppressive myeloid cells, including abundant macrophages, which contribute to T-cell exclusion (20–22), we assessed macrophage abundance and phenotype in these tumor tissues. We found that loss of GOT2 in cancer cells increased total macrophage abundance while decreasing the frequency of Arg1⁺ macrophages out of total macrophages (Fig. 2E), consistent with macrophage polarization to a less immune-suppressive phenotype permissive to T-cell recruitment. To further characterize the immune infiltrates of these tumors, we performed multiplex IHC (see Methods for details), which revealed relatively abundant Ki-67⁺CD8⁺ T cells (Fig. 2F) and CD11b⁺ myeloid cells (Supplementary Fig. S2G) in proximity to pan-cytokeratin⁺ tumor cells lacking GOT2 compared with controls. Quantification revealed that GOT2-null PDAC cells were associated with the increased presence of CD11b⁺PD-L1⁺ and CD11b⁺Ki-67⁺ cells (Supplementary Fig. S3A and S3B); increased presence of total TCF1/7⁺ and PD-1⁺ T cells as well as CD8⁺Ki-67⁺ and CD8⁺PD-1⁺Ki-67⁺ T cells; and increased trends for CD8⁺GRZB⁺ and CD8⁺PD-1⁺GRZB⁺ T cells, though these trends did not reach statistical significance (Supplementary Fig. S3C–S3H). To address whether the differences in T-cell abundance were secondary to differences in tumor size, we performed a time course and harvested tumors soon after transplantation to quantify intratumoral T cells. At 11 days after transplantation, a time point when tumors are small in control and sgGot2 tumors but not yet different in size (Supplementary Fig. S3I), T-cell frequencies were already increased in the GOT2-null setting (Fig. 2G); T-cell frequency was also increased at days 19 and 27 after transplantation, though tumors are different in size by these early time points. To further understand the impact of cancer cell-intrinsic GOT2 on the immune microenvironment, we analyzed the myeloid compartment of these tumors and identified pronounced changes to macrophage and dendritic cell populations including increases in proliferating macrophages and cDC1 (Supplementary Fig. S4A–S4M). We next asked whether these T cells were in fact functional in suppressing tumor progression. To address this, we treated control and sgGot2 tumors with depleting antibodies against CD4⁺ and CD8⁺ T cells. This intervention had no impact on the growth of control tumors, consistent with previous studies documenting a lack of T cell-mediated antitumor immunity in mouse models of PDAC (23). However, the growth of sgGot2 tumors was restored upon T-cell neutralization (Fig. 2H), indicating that GOT2 promotes PDAC progression at least in part by suppressing T cell-dependent antitumor immunity.

We next addressed the mechanism by which cancer cell-intrinsic GOT2 influences the immune microenvironment, taking potential enzymatic and fatty acid binding functions into account. To begin to address this, we examined GOT2 localization in PDAC cells and found that a pool of this

canonically mitochondrial protein localizes to the nucleus in murine premalignant lesions and PDAC as well as human PDAC *in vivo* (Fig. 3A and B; Supplementary Fig. S5A). We note that, although all human PDAC specimens examined showed evidence of nuclear GOT2 in pan-cytokeratin⁺ tumor cells, tumor cells with GOT2 restricted to mitochondrial and membrane-proximal regions and without nuclear GOT2 were also observed across these samples. This nuclear GOT2 pool was also evident *in vitro*, whether we analyzed endogenous or exogenous, His-tagged GOT2 (Supplementary Fig. S5B–S5E). We reasoned that the intact proliferation of GOT2-null tumors indicated the presence of metabolic adaptation mechanisms to retain redox balance, and this motivated us to consider noncanonical functions of GOT2 related to its putative fatty acid binding capacity. The previously unappreciated nuclear pool of GOT2 led us to hypothesize that GOT2 regulates nuclear trafficking of fatty acids either into or within the nucleus. Nuclear fatty acid trafficking has been reported to be regulated by fatty acid binding proteins (24, 25), and nuclear fatty acids have established functional significance as ligands for the peroxisome proliferator-activated receptor (PPAR) members of the nuclear receptor superfamily of transcription factors (26). This three-member family is activated by fatty acid ligands, and although PPAR α and PPAR γ display tissue-restricted expression and PPAR γ is downregulated during PDAC progression (27, 28), PPAR δ is ubiquitously expressed and was expressed in all PDAC lines examined whether or not GOT2 was inhibited (Supplementary Fig. S6A). Analysis of human PDAC RNA-seq data revealed a correlation between the expression of *GOT2* and the PPAR δ regulome (Fig. 3C; Supplementary Fig. S6B). Importantly, PPAR δ promotes tumorigenesis via tissue-specific metabolic and immunomodulatory mechanisms (29–32), prompting us to test a functional relationship between GOT2 and PPAR δ that may underlie the phenotypes of GOT2-null PDAC.

Transcriptional activity from a PPAR response element (PPRE) was reduced in GOT2-null PDAC cells (Fig. 3D), indicating that GOT2 positively regulates PPAR δ activity. Unlike steroid-activated nuclear receptors, which are sequestered in the cytoplasm in the absence of ligand and translocate to the nucleus upon ligand engagement, PPAR δ is constitutively nuclear and bound to DNA but undergoes a conformational change upon binding of nuclear fatty acids to enable interaction with coactivator complexes, altered DNA binding, and induction of target gene expression (33). Further supporting positive regulation of PPAR δ transcriptional activity by GOT2, nuclear extracts from control and sgGot2 cells were applied to wells containing immobilized, PPRE-containing DNA, followed by incubation with a PPAR δ antibody and a peroxidase-conjugated secondary antibody. Results of this assay indicated reduced PPAR δ transcriptional activity in GOT2-null PDAC cells (Fig. 3E). To identify immune-modulatory factors putatively regulated by the GOT2–PPAR δ axis, we performed a cytokine array on a conditioned medium from PDAC cells and found reductions in myeloid cell-modulating factors REG3G and M-CSF with GOT2 loss (Supplementary Fig. S6C and S6D) and thus included the associated genes in our analyses. Chromatin immunoprecipitation (ChIP) for PPAR δ and acetylated histone H3K9, a marker of active promoters, followed by qPCR also supported

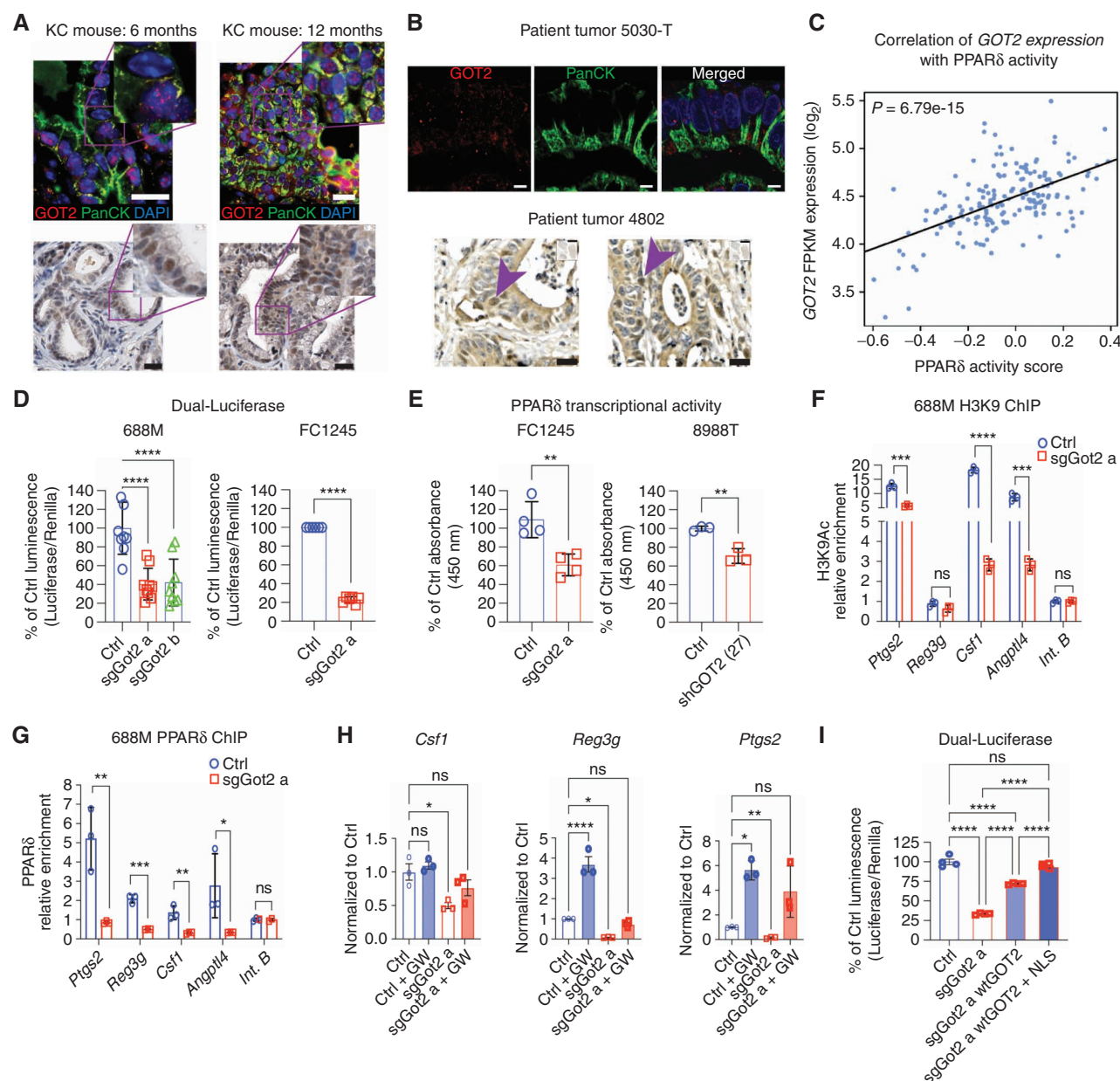


Figure 3. GOT2 positively regulates PPAR δ activity. **A**, IHC staining for GOT2 or GOT2 and panCK in pancreas tissues from *Kras*^{L5L-G12D/+};*Pdx1-Cre* (KC) mice at 6 or 12 months of age (representative of $n = 4$ per time point). Scale bars = 20 μ m. **B**, IHC staining for GOT2 or GOT2 and panCK in human PDAC (representative of $n = 5$). Fluorescent images: scale bar = 5 μ m, brightfield images: scale bar = 20 μ m. Arrowheads indicate examples of tumor cells with nuclear GOT2. **C**, Scatter plot depicting the correlation of *GOT2* expression with expression of PPAR δ target genes in human PDAC per TCGA RNA-seq data ($n = 177$). FPKM, fragments per kilobase of transcript per million mapped reads. **D**, Luciferase assay for PPRE activity in the indicated cell lines, normalized to Renilla, presented as mean \pm SEM. ****, $P < 0.0001$ by one-way ANOVA (688M) or an unpaired t test (FC1245). **E**, PPAR δ transcriptional activity assay, reading out binding to immobilized DNA containing PPREs, in the indicated cell lines. Data are presented as mean \pm SEM from four (FC1245) or three (8988T) independent experiments. **, $P < 0.01$ by an unpaired t test. **F** and **G**, ChIP for H3K9Ac (**F**) and PPAR δ (**G**) in control or sgGot2 688M PDAC cells, followed by qPCR for proximal promoter regions of the indicated genes. Data are normalized to an intergenic region (Int. B) and are presented as mean \pm SEM from biological triplicates. ns = not significant. *, $P < 0.05$; **, $P < 0.01$; ***, $P < 0.001$; ****, $P < 0.0001$ by an unpaired t test. **H**, qPCR for the indicated PPAR δ -regulated genes in control or GOT2-knockdown PDAC cells, treated with vehicle (DMSO) or the PPAR δ synthetic agonist GW501516 (GW; 100 nmol/L). Data are presented as mean \pm SEM from biological triplicates. ns = not significant. *, $P < 0.05$; **, $P < 0.01$; ****, $P < 0.0001$ by one-way ANOVA. **I**, Luciferase assay for PPRE activity in sgGOT2 PDAC cells reconstituted with wild-type GOT2 (wtGOT2) or NLS-wtGOT2. Data are presented as mean \pm SEM from four independent experiments. ns = not significant. ****, $P < 0.0001$ by one-way ANOVA. (continued on next page)

a reduction of PPAR δ transcriptional activity in the absence of GOT2 (Fig. 3F and G). Some of these genes previously linked to PPAR δ activity appear potentially to be indirect targets. Expression of PPAR δ target genes was also reduced in GOT2-null PDAC cells, and the synthetic PPAR δ agonist

GW501516 restored target gene expression, indicating that these genes are indeed regulated by PPAR δ (Fig. 3H). Among the genes with clear relevance to our *in vivo* phenotype was *PTGS2*, which encodes COX2. Recently reported gain- and loss-of-function experiments revealed that COX2 promotes

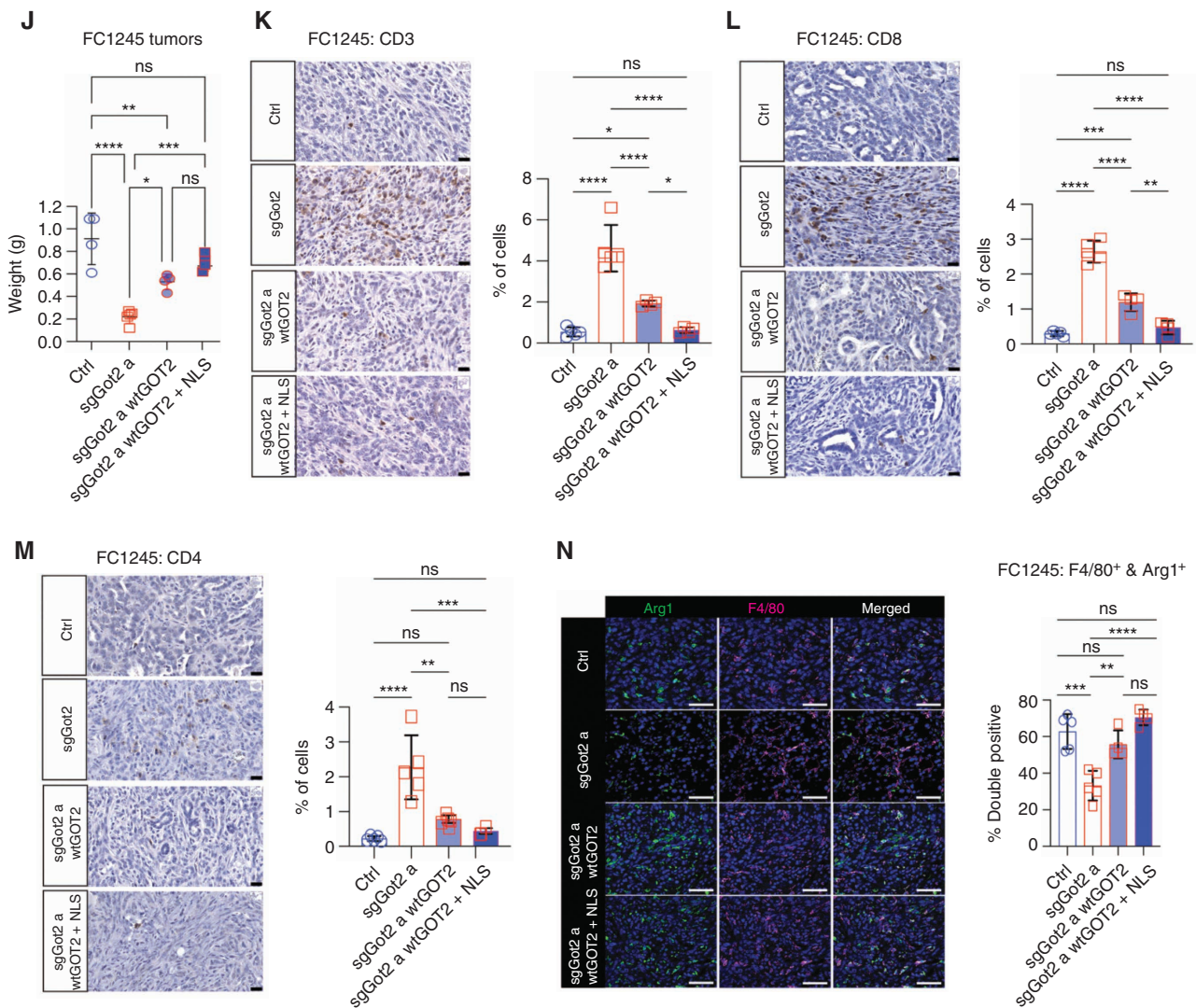


Figure 3. (Continued) **J**, PDAC tumor weight at the experimental endpoint, 22 days after orthotopic transplantation of FC1245 cells into immune-competent hosts ($n = 4-5$ per arm). Data are presented as mean \pm SEM. ns = not significant. *, $P < 0.05$; **, $P < 0.01$; ***, $P < 0.001$; ****, $P < 0.0001$ by one-way ANOVA. **K-M**, IHC staining and quantification of T-cell markers CD3, CD8, and CD4 in FC1245 tumors ($n = 4-5$ per arm, scale bars = 20 μm). Data are presented as mean \pm SEM. ns = not significant. *, $P < 0.05$; **, $P < 0.01$; ***, $P < 0.001$; ****, $P < 0.0001$ by one-way ANOVA. **N**, IHC staining and quantification of CD68 and Arg1 in FC1245 tumors ($n = 4-5$ per arm, scale bars = 20 μm). Data are presented as mean \pm SEM. ns = not significant. *, $P < 0.05$; **, $P < 0.01$; ***, $P < 0.001$; ****, $P < 0.0001$ by one-way ANOVA.

T-cell exclusion from the PDAC microenvironment, consistent with our results, and that *PTGS2* expression correlated with poor patient survival (34). *COX2* has also been implicated in the suppression of antitumor immunity in other cancer types (35). We further investigated the regulation of *COX2* downstream of *GOT2* and found that *COX2* protein levels were reduced in *GOT2*-null PDAC cells *in vitro* and *in vivo* (Supplementary Fig. S7A and S7B). Although *GOT2* lacks a nuclear localization sequence (NLS), we added an NLS to *GOT2* and found that increasing *GOT2* nuclear localization increased *PPAR δ* activity (Fig. 3I; Supplementary Fig. S7C). Although NLS-*GOT2* did not increase tumor growth compared with wild-type *GOT2* *in vivo*, increased *GOT2* nuclear targeting reduced T-cell abundance in these tumors, and Arg1⁺ macrophage abundance was not significantly altered (Fig. 3J-N; Supplementary Fig. S7D and S7E).

Reconstitution with wild-type *GOT2* restored immune suppression as expected, though CD8 T-cell abundance was not reduced all the way down to control levels (Fig. 3K-N). These results together support the hypothesis that *GOT2* promotes the transcriptional activity of *PPAR δ* in PDAC cells.

As we were prompted to investigate a *GOT2*-*PPAR δ* functional interaction based on the putative fatty acid binding function of *GOT2*, we investigated this role further. For this, we analyzed the crystal structure of human *GOT2* (36) and identified five putative fatty acid binding sites based on hydrophobicity (Fig. 4A and B). We then performed *in silico* docking studies for known fatty acid ligands for *PPAR δ* and identified a potential interaction between arachidonic acid and *GOT2* hydrophobic site 2 (Fig. 4C). This modeled interaction yielded a docking score of -7.6 kcal/mol, which is very similar to the docking score calculated for arachidonic acid in

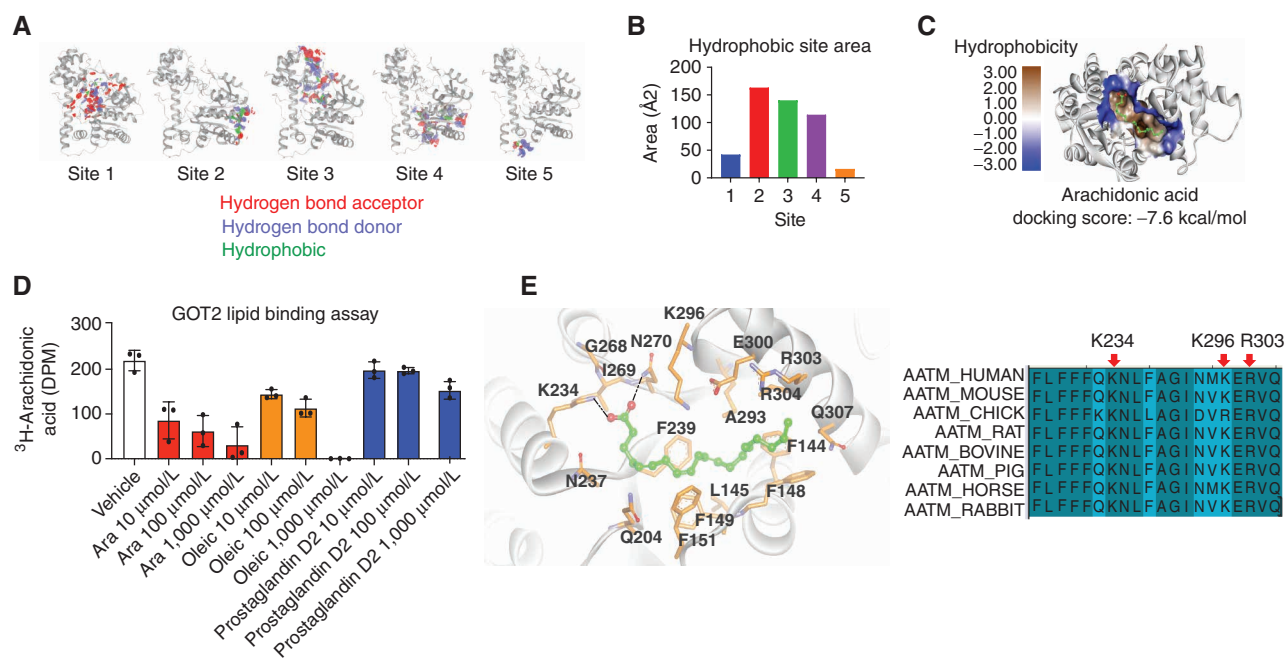


Figure 4. GOT2 binds to the PPAR δ ligand directly. **A**, Hydrophobic site maps on the GOT2 protein, indicating putative fatty acid binding domains. Red: hydrogen bond acceptor, blue: hydrogen bond donor, green: hydrophobic. **B**, Plot of the hydrophobic area of the putative fatty acid binding sites depicted in **A**. **C**, Docking model of arachidonic acid in site 2 on the GOT2 protein, with bioenergetic docking score (-7.6 kcal/mol) indicated below. **D**, Competitive fatty acid binding assay measuring radioactivity upon incubating purified human GOT2 with ³H-arachidonic acid (1 μ mol/L) and the indicated concentrations of cold lipid species. Ara, cold arachidonic acid. **E**, Left, model of arachidonic acid bound to GOT2, indicating amino acid residues that potentially facilitate binding. Based on this model, K234, K296, and R303 were selected for mutation to alanine. Right, conservation of GOT2 amino acid sequence, including the three residues predicted to support arachidonic acid binding, among higher vertebrates. (continued on next page)

the ligand binding domain of PPAR γ (-7.0 kcal/mol; ref. 37), an interaction that is known to be direct and functionally significant. To probe this interaction further, we performed competitive fatty acid binding assays using purified GOT2 protein and radiolabeled arachidonic acid. In addition to cold arachidonic acid, we used cold oleic acid, as this was previously reported to bind to GOT2 (ref. 10; though our analysis revealed a distinct fatty acid binding domain from this previous study) as well as prostaglandin D₂ (PGD₂), a downstream metabolite of arachidonic acid that we predicted to serve as a negative control and not to bind directly to GOT2 based on computational modeling. The competitive binding assay showed that arachidonic acid indeed bound to GOT2 directly, and although cold arachidonic acid readily displaced radiolabeled ligand, our negative control lipid (PGD₂) was unable to compete away the arachidonic acid signal even when PGD₂ concentration exceeded that of arachidonic acid by three orders of magnitude (Fig. 4D), supporting a specific interaction. Oleic acid had a modest effect on binding, suggesting that oleic acid may bind to the arachidonic acid-bound site but at a lower affinity or may bind to a separate site on the protein. To assess a relationship between GOT2 and arachidonic acid trafficking in cells, we performed mass spectrometry to measure arachidonic acid in whole cells and nuclei; levels were unchanged at the whole-cell level between control and sgGot2 cells (Supplementary Fig. S7F), but nuclear levels were below a reliable level of detection. We developed an assay to measure nuclear arachidonic acid accumulation by spiking fluorescent arachidonic acid into our culture medium and measuring fluorescent signal in isolated

nuclei, which revealed a reduction in nuclear arachidonic acid accumulation in two GOT2 loss-of-function cell lines (Supplementary Fig. S8A). Though significant, these differences were modest, suggesting that GOT2 may regulate arachidonic acid within the nucleus as opposed to predominantly regulating its nuclear import. To address the functional significance of GOT2 fatty acid binding, we looked closely at the putative fatty acid binding pocket we identified and selected three key amino acid residues that we predicted to be critical for arachidonic acid binding at that site (Fig. 4E). We note conservation of this amino acid sequence across mammalian species and between GOT1 and GOT2. We mutated these three residues on His-tagged GOT2 and used this triple-mutant GOT2 (tmGOT2) or wild-type GOT2 (wtGOT2) to reconstitute sgGot2 PDAC cells. Although wtGOT2 localized to mitochondria and nuclei, tmGOT2 exhibited a reduction in nuclear localization compared with the wild-type protein (Fig. 4F), raising the possibility that fatty acid binding at this site promotes GOT2 nuclear trafficking, perhaps via interaction with a chaperone. To further probe the relationship between nuclear GOT2 and PPAR δ , we immunoprecipitated GOT2 from whole cells and found that wtGOT2 interacts with PPAR δ , whereas this interaction is reduced upon disruption of fatty acid binding (Fig. 4G). After confirming that tmGOT2 retains enzymatic activity (Supplementary Fig. S8B and S8C), we assessed PPAR δ activity and found that target gene expression and transcriptional activity were reduced in cells expressing tmGOT2 compared with wtGOT2 (Fig. 4H and I). We next transplanted immune-competent mice with control, sgGot2, sgGot2 + wtGot2, or sgGot2 + tmGot2

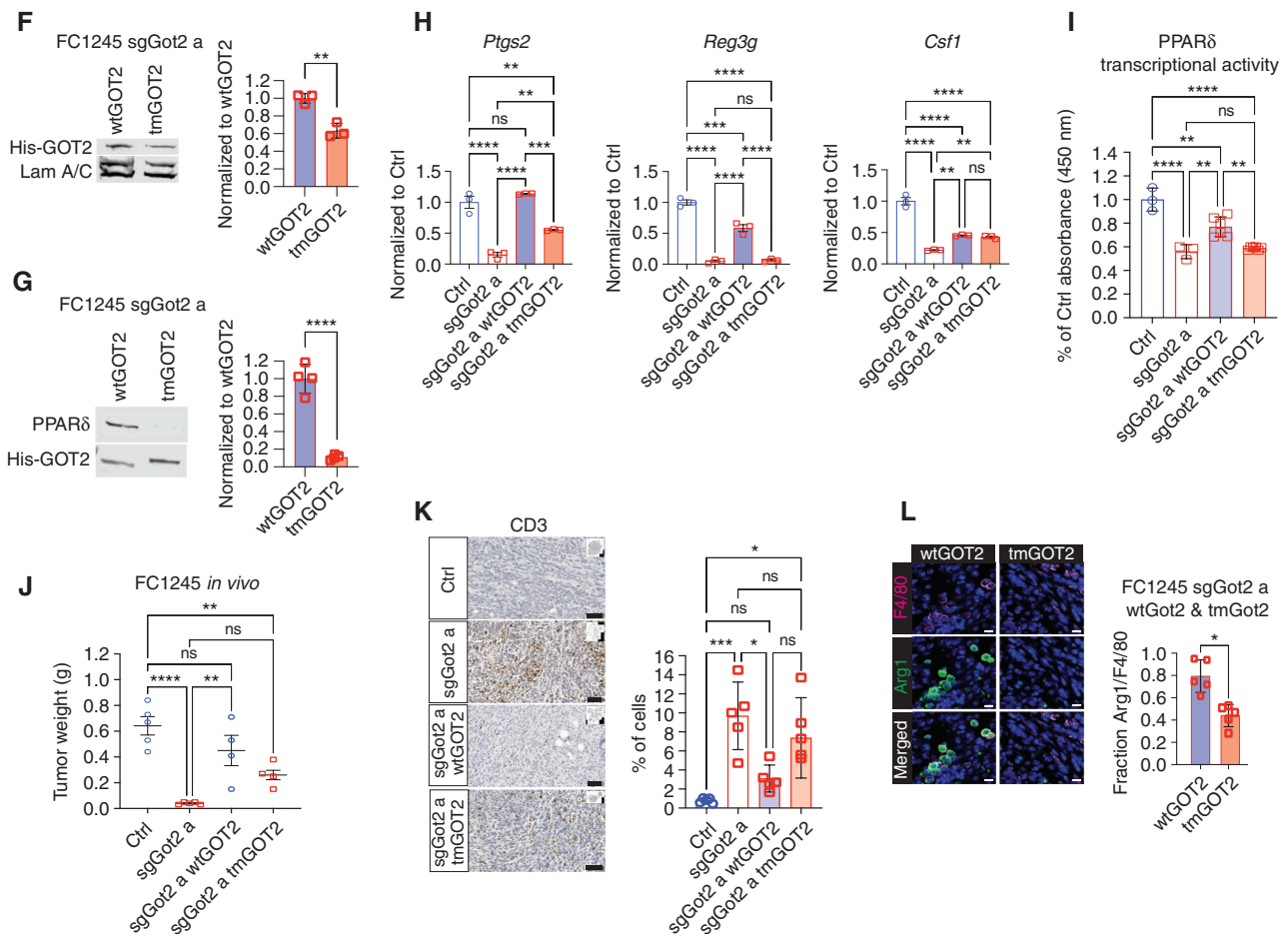


Figure 4. (Continued) **F**, Western blots indicating nuclear and whole-cell abundance of wtGOT2 and tmGOT2 (both His-tagged) in reconstituted sgGOT2 FC1245 PDAC cells. Nuclear GOT2 quantification appears to the right. **, $P < 0.01$ by an unpaired t test. **G**, Western blots from whole-cell lysates or His pulldowns from the cells depicted in **F**. ****, $P < 0.0001$ by an unpaired t test. **H**, qPCR for the indicated PPAR δ -regulated genes in FC1245 stable cell lines, normalized to *36b4*. Data are presented as mean \pm SEM from biological triplicates. ns = not significant. **, $P < 0.01$; ***, $P < 0.001$; ****, $P < 0.0001$ by one-way ANOVA. **I**, PPAR δ transcriptional activity assay in the indicated FC1245 stable cell lines. Data are presented as mean \pm SEM from three to six biological replicates. ns = not significant. **, $P < 0.01$; ****, $P < 0.0001$ by one-way ANOVA. **J**, PDAC tumor weight at the experimental endpoint, 18 days after orthotopic transplantation of the indicated FC1245 cells. Ctrl: $n = 5$, sgGot2 a: $n = 5$, sgGot2 a + wtGOT2: $n = 4$, sgGot2 a + tmGOT2: $n = 5$. Ctrl and sgGot2 arms here are also depicted in Fig. 1E. Data are presented as mean \pm SEM. ns = not significant. **, $P < 0.01$; ****, $P < 0.0001$ by one-way ANOVA. **K** and **L**, IHC staining (scale bars = 50 μ m) and quantification for T cells (**K**: CD3) and macrophages (**L**: F4/80 and Arg1) in PDAC harboring wtGOT2 or tmGOT2 ($n = 5$ per arm). Data are presented as mean \pm SEM. ns = not significant. *, $P < 0.05$; ****, $P < 0.001$ by one-way ANOVA (**K**) or an unpaired t test (**L**).

PDAC cells. We noted that wtGot2 had a strong nuclear localization *in vivo*, whereas tmGot2 was heterogeneous, with strong nuclear signal in some cells and a diffuse staining pattern in others (Supplementary Fig. S8D). Although wtGot2 completely rescued tumor growth as expected, tmGot2 only partially rescued tumor growth (Fig. 4J) and immune suppression (Fig. 4K and L). Disruption of GOT2 transaminase activity (1) did not affect tumor growth (Supplementary Fig. S9A–S9C). To further test the importance of enzymatic activity for the nuclear function of GOT2, we treated inducible shGOT2 8988T PDAC cells, sensitive to acute GOT2 inhibition with respect to proliferation, with the pan-transaminase inhibitor aminoxyacetate (AOA; ref. 38). We found that although AOA reduced the proliferation of these cells, transaminase inhibition had no impact on PPAR δ activity (Supplementary Fig. S9D–S9G). Together, these results indicate a significant role for the fatty acid binding region in GOT2-mediated PDAC progression.

Based on these results, we hypothesized that PPAR δ activation would restore PDAC growth in the GOT2-null setting. We treated PDAC cells with GW501516, as we found this to override the limitation on PPAR δ activity in GOT2 cells *in vitro*, and observed no increase (in fact, a decrease) in proliferation (Fig. 5A). However, GW501516 treatment *in vivo* rescued the growth of GOT2-null PDAC without impacting control tumor growth (Fig. 5B) and restored immune suppression with respect to intratumoral T-cell abundance (Fig. 5C) and induction of COX2 expression (Fig. 5D). As GW501516 acts systemically, we next specifically activated PPAR δ in PDAC cells by introducing a fusion of PPAR δ with the VP16 transactivation domain from herpes simplex virus (39), to enable ligand-independent activation, into control and sgGot2 PDAC cells (Supplementary Fig. S10A) at sufficiently low copy number to avoid detectable PPAR δ overexpression. Although VP16-PPAR δ increased neither proliferation *in vitro* (Fig. 5E) nor PDAC growth in the control

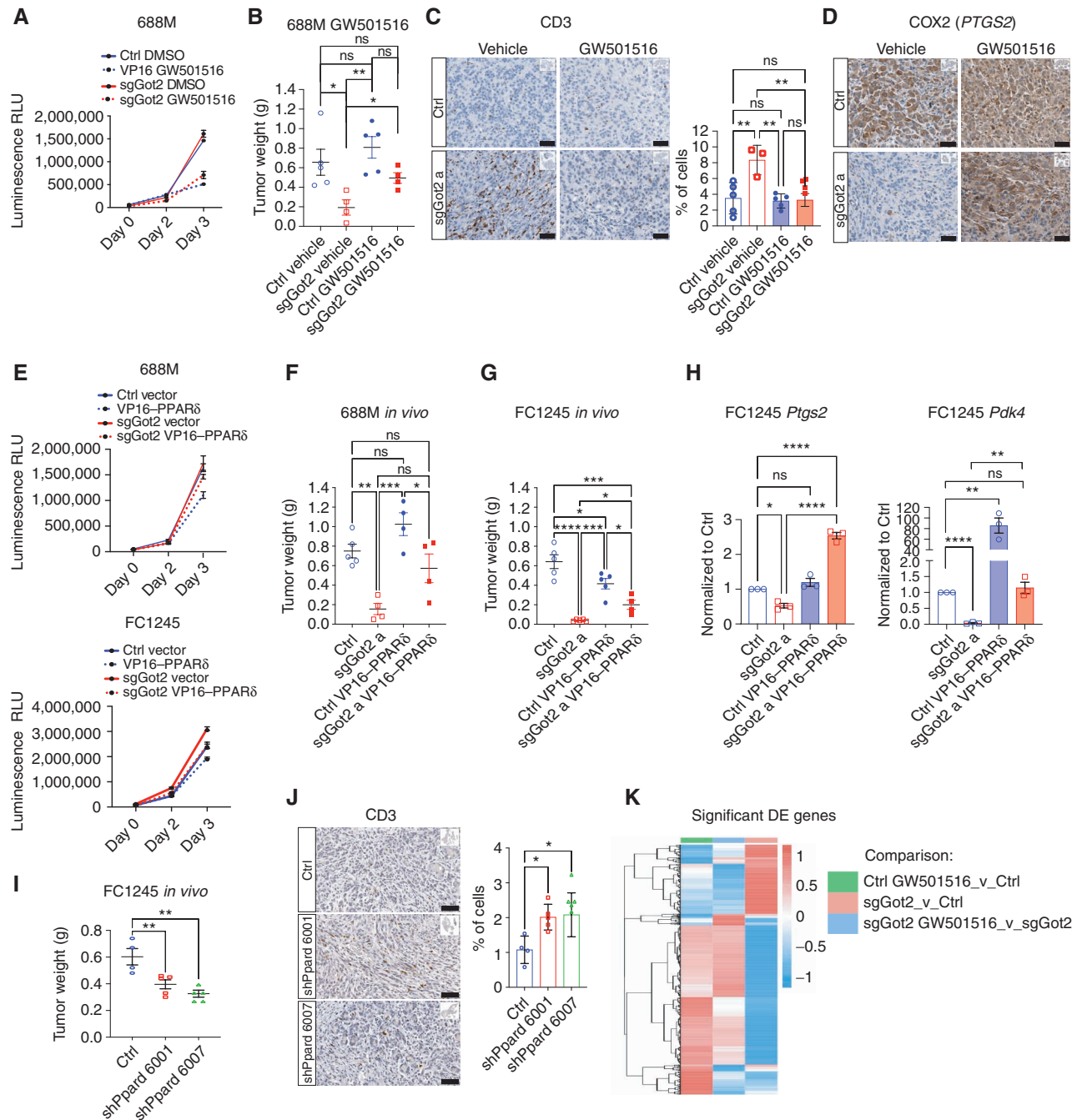
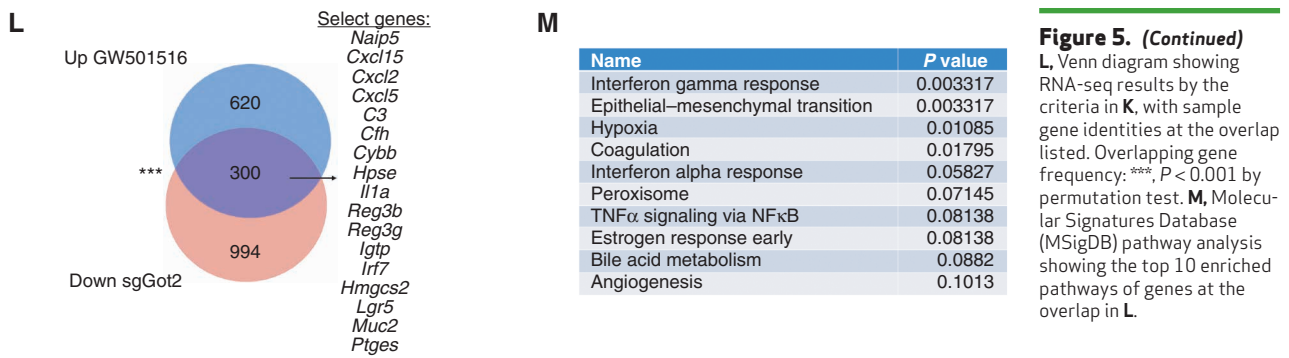


Figure 5. PPAR δ activation restores tumor growth and T-cell exclusion in the absence of GOT2. **A**, Viable cell measurements in control or sgGot2 PDAC cells treated with vehicle or 100 nmol/L GW501516. RLU, relative light unit. **B**, PDAC tumor weight at the experimental endpoint, 30 days after orthotopic transplantation of the control or sgGot2 cells, with daily i.p. injection of vehicle or 4 mg/kg GW501516. Ctrl: $n = 5$ per cohort, sgGot2: $n = 4$ per cohort. Data are presented as mean \pm SEM. ns = not significant. * $P < 0.05$; ** $P < 0.01$ by one-way ANOVA. **C**, IHC staining of control and sgGot2 688M tumors treated with vehicle or GW501516 as in **B** for the T-cell marker CD3. Representative images are shown above (scale bars = 50 μ m), with quantification below (ctrl: $n = 5$, ctrl + GW501516: $n = 5$, sgGot2: $n = 3$, sgGot2 + GW501516: $n = 4$). Data are presented as mean \pm SEM. ns = not significant. ** $P < 0.01$ by one-way ANOVA. **D**, IHC staining for PTGS2/COX2 in control or sgGot2 PDAC treated with vehicle or GW501516 (representative of $n = 3$ -5 per cohort). Scale bars = 50 μ m. **E**, Viable cell measurements in control or sgGot2 PDAC cells stably transduced with empty vector or VP16-PPAR δ . Data are presented as mean \pm SEM. **F** and **G**, PDAC tumor weight at the experimental endpoint in the indicated 688M (**F**) and FC1245 (**G**) lines. 688M: Ctrl: $n = 5$, sgGot2 a: $n = 4$, ctrl VP16-PPAR δ : $n = 4$, sgGot2 a VP16-PPAR δ : $n = 4$, endpoint = day 27. FC1245: Ctrl: $n = 5$, sgGot2 a: $n = 5$, ctrl VP16-PPAR δ : $n = 5$, sgGot2 a VP16-PPAR δ : $n = 4$, endpoint = day 18. Ctrl and sgGot2 FC1245 arms here are also depicted in Fig. 1E. ns = not significant. * $P < 0.05$; ** $P < 0.01$; *** $P < 0.001$; **** $P < 0.0001$ by one-way ANOVA. **H**, qPCR for PPAR δ -regulated genes in the indicated FC1245 stable cell lines, normalized to *36b4*. Data are presented as mean \pm SEM from biological triplicates. * $P < 0.05$; ** $P < 0.01$; **** $P < 0.0001$ by one-way ANOVA. **I**, PDAC tumor weight at experimental endpoint (day 18) in ctrl ($n = 4$) and shPpard ($n = 5$ per hairpin) FC1245 tumors. ** $P < 0.01$ by one-way ANOVA. **J**, Quantification of CD3 IHC on the tumors from **I** (scale bars = 50 μ m). ns = not significant. * $P < 0.05$ by one-way ANOVA. **K**, Heat map depicting differentially expressed (DE) genes in control and sgGot2 FC1245 PDAC cells, untreated or treated with 500 nmol/L GW501516 for 24 hours ($n = 3$ per group), identified by RNA-seq using cutoff criteria $P_{adj} < 0.01$ and $\log_2FC < -1$ or > 1 in at least one comparison. (continued on next page)

**Figure 5. (Continued)**

L, Venn diagram showing RNA-seq results by the criteria in **K**, with sample gene identities at the overlap listed. Overlapping gene frequency: ***, $P < 0.001$ by permutation test. **M**, Molecular Signatures Database (MSigDB) pathway analysis showing the top 10 enriched pathways of genes at the overlap in **L**.

group, genetic PPAR δ activation significantly albeit partially rescued tumor growth in sgGot2 tumors in two independent models (Fig. 5F and G). Consistent with these findings, VP16–PPAR δ increased expression of target genes such as *Ptgs2* in sgGot2 cells (Fig. 5H). PPAR δ knockdown in PDAC cells similarly reduced tumor growth and immune suppression (Fig. 5I and J; Supplementary Fig. S10B). Motivated by these results, we performed RNA-seq on control and sgGot2 PDAC cells treated with GW501516 to understand the transcriptional programs regulated by GOT2 and PPAR δ . Genes downregulated with loss of GOT2 were enriched for inflammatory mediators and for genes upregulated by PPAR δ agonist in macrophages in a previous study (40), whereas genes upregulated by PPAR δ agonist and downregulated with GOT2 loss within PDAC cells overlapped significantly and genes in the overlap were enriched for immune-modulatory genes (Fig. 5K–M; Supplementary Fig. S11A–S11C). Genes in the overlap included classic PPAR δ target genes, such as *Hmgcs2*, as well as targets identified in this study, such as *Reg3g*. Together, these results indicate that GOT2 promotes PDAC progression and immune suppression by activating PPAR δ .

DISCUSSION

Our study indicates that GOT2 plays a critical role in promoting a tumor-permissive immune microenvironment in the pancreas. This function is attributable at least in part to direct fatty acid binding and activation of nuclear receptor PPAR δ . GOT2 loss did not affect the whole-cell abundance of any of the fatty acids measured, supporting a mechanism functionally downstream of fatty acid uptake. That said, analysis of our RNA-seq results for expression of fatty acid transporters (FATP1–6 encoded by *SLC27a1–6*, CD36) showed that *Slc27a1* (encoding FATP1) was significantly downregulated with loss of GOT2, raising the possibility that uptake of other fatty acids may be indirectly affected by GOT2. The same transporter, *Slc27a1*, was significantly upregulated by PPAR δ agonism, consistent with transcriptional regulation by a GOT2–PPAR δ axis. Although diverse impacts on the tumor immune contexture resulted from perturbation of the GOT2–PPAR δ axis, the increased infiltration of cDC1 into tumors lacking cancer cell–intrinsic GOT2 was particularly promising in light of recent studies demonstrating the paucity of dendritic cells in PDAC as a cause of immune suppression (41, 42). Conversely, their increase in the GOT2-null setting is consistent with and may indeed enable antitumor immunity, which should be tested directly in future studies. Our results

agree with a recent study showing that dietary or pharmacologic activation of PPAR δ cooperates with oncogenic KRAS to drive pancreatic tumorigenesis by promoting immune-suppressive changes to the myeloid compartment (43). We note that our studies made use of orthotopic, syngeneic models of PDAC. Although these models have meaningful strengths relevant to human PDAC including an immune-suppressive phenotype and reflect the genetically engineered, spontaneous models from which they were derived with respect to the lack of T cell–mediated antitumor immune response in control mice, these models also present limitations. For example, these models do not progress through relevant stages of premalignant lesions, and our study leaves in question the significance of GOT2 in regulation of the immune microenvironment and disease progression in early neoplasia, which will best be addressed in spontaneous models of PDAC.

Further studies are needed to understand the mechanisms regulating GOT2 subcellular localization, the precise molecular mechanism by which GOT2 promotes PPAR δ transcriptional activity, and whether this functional interaction extends beyond pancreatic cancer cells. This last point is poised for investigation thanks to the recent development of a *Got2-flox* mouse strain (44). Motivated by such studies, analysis of GOT2 expression across tissues shows the highest expression in tissues known to be functionally regulated by PPAR δ , including skeletal muscle, heart, and liver (<https://gtexportal.org/home/>). We speculate that the normal function of this GOT2–PPAR δ axis is to provide high levels of localized fatty acid ligand directly to constitutively nuclear PPAR δ via GOT2 fatty acid binding and transient nuclear shuttling into proximity of PPAR δ , which we expect occurs at specific but not all PPAR δ binding sites in light of our transcriptional profiling results. Investigating the therapeutic potential of targeting this GOT2–PPAR δ axis is an appealing next step. With this goal in mind, we note that GOT2 has been subject to little characterization or functional study in immune cells directly. That said, analysis of publicly available RNA-seq data from human immune cell subsets showed that whereas GOT2 expression is low in most cell types examined, expression is appreciable in naïve CD4 and CD8 T cells (<https://dice-database.org/>). This gains potential significance in light of a recent study showing that exogenous GOT2 expression increased antitumor activity of CAR T cells in preclinical models, which was attributed to GOT2 metabolic function (45). Together with our findings, these results raise the possibility that therapeutic strategies parsing the enzymatic and fatty acid binding functions may be important. Although diverse mechanisms contribute to

immune evasion in PDAC (46), targeting GOT2 may be part of a potential treatment approach to foster an immune response against this deadly cancer.

METHODS

Animals

All experiments were reviewed, approved, and overseen by the institutional animal use and care committee at Oregon Health & Science University (OHSU) in accordance with NIH guidelines for the humane treatment of animals. C57BL/6J (000664, for models with FC1245; ref. 47) or B6129SF1/J (101043, for models with 688M; ref. 48) mice from The Jackson Laboratory were used for orthotopic transplant experiments at 8 to 10 weeks of age. Tissues from 6- or 12-month-old *Kras*^{LSL-G12D/+}; *Pdx1-Cre* (KC) mice were kindly provided by Dr. Ellen Langer (OHSU).

Human Tissue Samples

Human patient PDAC tissue samples donated to the Oregon Pancreas Tissue Registry program (OPTR) in accordance with full ethical approval were kindly shared by Dr. Jason Link and Dr. Rosalie Sears (OHSU), and written informed consent from patients was received for all human tissue samples used in this study.

Plasmids

The pCMX-VP16-PPARD plasmid was kindly provided by Dr. Vihang Narkar (University of Texas Health Science Center at Houston; ref. 39). The VP16-PPARD element was cloned into the lentiviral vector. To construct pLenti VP16 PPARD, the VP16-PPARD element was amplified by PCR using sense primer 5'-GGGGACAAGTTTG TACA AAAAAGCAGGCTTAATGGCCCCCCCCGAC-3' and antisense primer 5'-GGGGACCACCTTTGTACAAGAAAGCTGGGTTTTAGTAC ATGTCCTGTAGATTTCCTGGAGCAGG-3'. PCR product was inserted into pDONR 221 entry clone using Gateway BP Clonase II enzyme (Thermo Fisher 12535029). Entry clone VP16 PPARD element was swapped into the expression region of pLenti CMV Puro DEST (Addgene #17452) using LR Clonase II enzyme (Thermo Fisher 11-791-020) to generate the pLenti VP16 PPARD construct. The pCMV3 plasmid containing C-terminal His-tagged human GOT2 cDNA was purchased from Sino Biological (HG14463-CH) and cloned into the lentiviral vector pLenti CMV Puro DEST (Addgene #17452) using the same approach as pLenti VP16 PPARD. pLenti wtGOT2 PCR product was generated using sense primer 5'-GGGGACAAGTTTG TACAAAA AAGCAGGCTTAATGGCCCTGCTGCACT-3' and antisense primer 5'-GGGGACCACCTTTGTACAAGAAAGCTGGGTTTTAGTGTATGGT GGTGATGATGGTGG-3'. Triple-mutant GOT2 was constructed using the Q5 Site-Directed Mutagenesis Kit (New England Biolabs E0552S) in two subsequent steps. Two sets of primers were used to generate three site mutations: primer set 1 for K234A mutation (F: 5'-AACAGTGGTG GCGAAAAGGAATCTC-3'; R: 5'-GCTATTCCTTCCACTGTTC-3') and primer set 2 for K296A and R303A mutations (F: 5'-GTCTG CGCAGATGCGGATGAAGCCAAAGCGGTAGA GTC-3'; R: 5'-CATA GTGAAGG CTCCTACACG-3'). pLenti tmGOT2 was then generated using the same approach and primers as pLenti wtGOT2. pLenti aspartate transaminase mutant GOT2 (atamGOT2) was constructed in two consecutive steps using pLenti wtGOT2 as a template, with point mutations selected based on a human genetics study (1). The first step generated the R262A mutant using primers F: 5'-CTGTGGGCCACTTCATCGAA-3' and R: 5'-CCCAGGCATCCTTA TCACCATC-3'. The second step added the R337G mutant to the existing R262A mutant using primers F: 5'-CCAGATTTGG GAAAACAATGGC-3' and R: 5'-GGTGTTCAGAATGGCAGCA-3'. The pLenti NLS wtGOT2 construct was generated by inserting one cMYC NLS sequence into the C-terminus region using sense primer 5'-GTGAAACTGGATCTCGAGGGAGGCTCTCACCATC-3' and antisense primer 5'-TCTCTTAGCAGCAGGACCCCCCTTGGTGG-3'.

Cell Lines

Human pancreatic cancer cell lines MIA PaCa-2, PA-TU-8988T, Panc1, HPAF-II, and Capan-2 were obtained from ATCC and grown in Dulbecco's modified Eagle medium (DMEM) containing 10% FBS. Nontransformed, TERT-immortalized human pancreatic ductal epithelial cells were kindly provided by Dr. Rosalie Sears (OHSU; ref. 49). PA-TU-8988T cells harboring doxycycline-inducible shGOT2 were kindly provided by Dr. Costas Lyssiotis (University of Michigan). FC1245 PDAC cells were generated from a primary tumor in *Kras*^{LSL-G12D/+}; *Trp53*^{LSL-R172H/+}; *Pdx1-Cre* mice and were kindly provided by Dr. David Tuveson (Cold Spring Harbor Laboratory; ref. 47). 688M PDAC cells were generated from a liver metastasis in *Kras*^{LSL-G12D/+}; *Trp53*^{LSL-R172H/+}; *Pdx1-Cre*; *Rosa26*^{LSL-tTomato/+} mice and were kindly provided by Dr. Monte Winslow (Stanford University School of Medicine; ref. 48). Cell lines were routinely tested for *Mycoplasma* at least monthly (MycoAlert Detection Kit, Lonza).

The pSpCas9(BB)-2A-Puro(PX459) v2.0 plasmid (Addgene #62988) was used to clone guide sequences targeting *Got2* per the supplier's protocol: sgRNA A: GACGCGGGTCCACGCCGGT, sgRNA B: ACG CGGGTCCACGCCGGTG. The 688M or FC1245 cell line was transfected with a control plasmid or plasmid containing either of the sgGot2 sequences and subject to selection with 2 μ g/mL puromycin for 4 days. Single-cell clones were expanded and screened for GOT2 protein expression by Western blot.

GOT2 shRNA vectors were purchased in bacterial glycerol stocks from Sigma-Aldrich Mission shRNA (mouse shRNA A: TRCN0000325948, shRNA B: TRCN00000325946; human sh24: TRCN0000034824, sh27: TRCN0000034827), as were PPARD shRNA vectors (shRNA 6001: TRCN0000026001, shRNA 6007: TRCN0000026007). Briefly, bacterial cultures were amplified in an ampicillin growth medium from glycerol stocks for use in the purification of plasmid DNA. Subsequently, the purified plasmid was transfected to packaging cells HEK293T for the production of lentiviral particles. FC1245 cells were then infected and puromycin selected to generate stable GOT2 or PPARD knockdowns, with validation by Western blot. Lentivirus preparation for stable cell line generation was done with pMD2.G envelope plasmid (Addgene #12259) and psPAX2 packaging plasmid (Addgene #12260) in 293T-LentiX cells. Briefly, 5 μ g of pMD2.G, 5 μ g of psPAX2, and 10 μ g of plasmid DNA (shGOT2 KD, shPPARD KD, VP16-PPARDdelta, wtGOT2, tmGOT2, NLS-wtGOT2, atamGOT2, or scramble ctrl) were combined with 600 μ L Opti-MEM and 20 μ L lipofectamine 2000 for 20 minutes at room temperature. Dishes (10 cm) of 293T-LentiX were kept in 0% FBS DMEM, and the mixture was added in a dropwise manner. Twelve hours later, media were changed to 10% FBS DMEM. At 24 and 48 hours after transduction, media were collected and filtered through a 0.25- μ m filter, aliquoted, and frozen at -80°C. For lentiviral transduction of human and mouse cell lines, cells were plated to 6-well plates. Polybrene (10 μ g/mL; EMD Millipore TR-1003-G) was added to 1 mL 10% FBS DMEM and 300 μ L of filtered lentivirus media. Twenty-four hours later, media were changed to a fresh 10% FBS DMEM. Forty-eight hours after initial transduction, cells were treated with 2 μ g/mL puromycin (Thermo Fisher A1113803) or 4 μ g/mL puromycin depending on the cell line. A control well of nontransduced cells was used as an indicator for proper selection. Protein knockdown was validated by Western blot. For transaminase inhibition *in vitro*, AOA (Millipore Sigma; C13408) was used at 1 mmol/L as previously described (50).

Western Blotting

PDAC cells were treated as described in the text, and whole-cell lysates were prepared in RIPA buffer containing protease inhibitor cocktail (Sigma-Aldrich 11836170001). Alternatively, subcellular fractions were prepared using the Cell Fractionation Kit #9038 purchased from Cell Signaling Technology following the manufacturer's instructions. Briefly, cells were collected with scraping, washed in PBS, and

pelleted ($350 \times g$ 5 minutes). Cells were resuspended in 500 μ L PBS and 100 μ L reserved for whole-cell lysis in RIPA buffer + cOmplete mini EDTA-free protease inhibitor cocktail. The remaining cell pellet was centrifuged ($500 \times g$ 5 minutes), PBS was decanted, and 500 μ L CIB + 5 μ L protease inhibitor and 2.5 μ L PMSF was added. Solutions were vortexed and stored on ice for 5 minutes. Lysates were centrifuged ($500 \times g$ 5 minutes); the supernatant was collected as the cytosolic fraction. The remaining insoluble pellet was washed with CIB, and the supernatant was decanted. MIB (500 μ L) + 5 μ L protease inhibitor and 2.5 μ L PMSF was then added to the cell pellet. After vortexing for 15 seconds, solutions were incubated on ice for 5 minutes and centrifuged ($8,000 \times g$ 5 minutes). The supernatant was collected as the membrane and organelle fraction. Pellet was then washed in MIB, and the supernatant was decanted. CyNIB (250 μ L) + 2.5 μ L protease inhibitor + 1.25 μ L PMSF was then added to the pellet containing nuclei. The solution was sonicated for 5 seconds at 20% power $3\times$ to prepare nuclear lysate. For Western blot, 60 μ L $4\times$ LDS loading buffer with $10\times$ reducing agent was added for every 100 μ L of supernatant per fraction. Samples were boiled for 5 minutes at 95°C and centrifuged for 3 minutes at $15,000 \times g$; 15 μ L of each fraction along with 15 μ L of the whole-cell lysate was loaded for Western blotting. Alternatively, to generate total nuclear and cytosolic fractions, NE-PER Nuclear and Cytoplasmic Extraction Reagent Kit (Thermo Fisher) was used according to the manufacturer's protocol. Where indicated, His-tagged GOT2 protein was immunoprecipitated using the His-tag isolation and pulldown Dynabeads system (Thermo Fisher) using the manufacturer's protocol. Protein concentration was quantitated using the BCA Protein Assay Kit (Pierce). Equal amounts of protein were loaded in each lane and separated on a 4% to 12% Bis-Tris NuPAGE gel (Invitrogen), and then transferred onto a PVDF membrane. Membranes were probed with primary antibodies and infrared secondary antibodies: GOT2 (Thermo Fisher PA5-77990), β -Actin (Santa Cruz sc-47778), PPAR δ (Abcam ab178866), His (R&D Systems MAB050-100), COX2 (Abcam ab15191), COX IV (Cell Signaling Technology 11967S), AIF (Abcam ab1998), PMCA1 (Novus Biologicals 5F10), Lamin A/C (Cell Signaling Technology 4777S), Tom20 D8T4N (Cell Signaling Technology 42606S), HSC 70 (Santa Cruz sc-7298), Cas9 (Novus Biologicals NBP2-36440SS), GOT1 (Sigma-Aldrich AV48205), anti-rabbit Alexa Fluor Plus 680 (Thermo Fisher A32734), and anti-mouse Alexa Fluor Plus 800 (Invitrogen A32730). Protein bands were detected using the Odyssey CLx infrared imaging system (LI-COR Biosciences).

Immunofluorescence

Cells plated on coverslips were fixed in 10% neutral buffered formalin for 10 minutes at room temperature, washed three times with PBS, and permeabilized with 0.1% Triton X-100 for 10 minutes at room temperature. When MitoTracker staining was performed, cells plated on coverslips were stained with 100 nmol/L MitoTracker (Thermo Fisher M22462) at 37°C for 15 minutes prior to fixation. Following permeabilization, coverslips were blocked for 1 hour at room temperature in blocking solution (Aqua block buffer, Abcam ab166952) and then transferred to a carrier solution (Aqua block) containing diluted primary antibodies: GOT2 (Sigma-Aldrich HPA018139), COX IV (Cell Signaling Technology 11967S), COX2 (Abcam ab15191), and His (R&D Systems MAB050-100). Coverslips were incubated with the primary antibody at 4°C overnight and then washed five times for 5 minutes each in PBS, following which secondary Alexa Fluor-conjugated antibodies diluted in the same carrier solution (1:400) were added to the coverslips for 1 hour at room temperature. After the secondary antibody incubation, coverslips were washed five times for 5 minutes each in PBS and mounted with Vectashield mounting media containing DAPI (Vector Laboratories; H-1500). Images were captured on a Zeiss LSM 880 laser-scanning inverted confocal microscope at the OHSU Advanced Light Microscopy Shared Resource, and a $40\times/1.1$ NA water objective or $63\times/1.4$ NA oil objective was used to image the samples.

IHC

Mice were anesthetized and euthanized according to institutional guidelines. Pancreatic tumors were excised carefully and fixed overnight in 10% phosphate-buffered formalin. Tissue samples were paraffin-embedded and sectioned by the OHSU Histopathology Shared Resource. Human PDAC tissue sections from formalin-fixed, paraffin-embedded blocks were obtained from the OPTR. In brief, tissue sections were deparaffinized and rehydrated through an ethanol series and ultimately in PBS. Following antigen retrieval, tissue samples were blocked for 1 hour at room temperature in a blocking solution (8% BSA solution) and then transferred to a carrier solution (8% BSA solution) containing diluted antibodies: GOT2 (Sigma-Aldrich HPA018139), COX IV (Cell Signaling Technology 11967S), COX2 (Abcam ab15191), CD3 (Abcam ab5690), CD4 D7D2Z (Cell Signaling Technology 25229S), CD8 (Abcam ab203035), F4/80 (Cell Signaling Technology 70076T), and Arginase-1 (ARG1; Sigma-Aldrich ABS535). Sections were incubated overnight at 4°C and then washed five times for 5 minutes each in PBS. For fluorescence imaging, secondary Alexa Fluor-conjugated antibodies diluted in the same carrier solution (1:400) were added to the sections for 1 hour at room temperature. Sections were then washed five times for 5 minutes each in PBS and were mounted with Vectashield mounting media containing DAPI. For DAB chromogen imaging, sections were stained with primary antibody as described above, then the samples were incubated in polymeric horseradish peroxidase (HRP)-conjugated secondary antibody (Leica PV6121) for 1 hour, followed by five 5-minute $1\times$ TBST washes. HRP was detected using DAB chromogen (3,3'-diaminobenzidine) solution (BioCare Medical BDB2004) prepared per the manufacturer's instructions. Tissues were exposed to chromogen solution until a brown precipitate was detected produced from oxidized DAB where the secondary poly-HRP antibody is located. As soon as DAB chromogen was detected, tissue slides were washed in dH_2O , counterstained in hematoxylin, dehydrated, and cleared for mounting. Stained tissue sections were scanned on a Leica Biosystems Ariol digital fluorescence scanner or Leica Biosystems Aperio brightfield digital scanner. Quantification was performed for single stains using QuPath quantitative pathology and bioimage analysis software v0.2.3. For costains (CD8/GRZB and F4/80/ARG1), manual counting was performed on at least 10 high-powered fields per tumor sample.

Multiplex IHC

Sequential IHC was performed on 5- μ m formalin-fixed, paraffin-embedded sections as previously described (51, 52). Briefly, slides were deparaffinized, which was followed by heat-mediated antigen retrieval in pH 6.0 Citra solution (BioGenex HK086) followed by blocking in Dako Dual Endogenous Block (Dako S2003) and then 10 minutes of protein blocking with 5% normal goat serum and 2.5% BSA in TBST. Primary antibodies were applied in sequential order as listed in Box 1. After washing off primary antibody in TBST, either anti-rat (414311F), anti-mouse (414131F), or anti-rabbit (414141F) Histofine Simple Stain MAX PO HRP-conjugated polymer (Nichirei Biosciences) was applied for 30 minutes at room temperature, followed by AEC chromogen (Vector Laboratories SK-4200). Whole-slide digital imaging was performed following each chromogen development. Heat and chemical stripping between cycles and rounds was performed as previously described (51, 52). DNA was stained with hematoxylin (Dako S330130-2) for the purposes of image computation.

Regions of interest were selected, and then images were coregistered in MATLAB version R2018b using the SURF algorithm in the Computer Vision Toolbox (The MathWorks, Inc.). Image processing and cell quantification were performed using FIJI (53) and CellProfiler Version 3.5.1 (54). AEC signal was extracted for quantification and visualization in FIJI using a custom macro for color deconvolution. Briefly, the FIJI plugin Color_Deconvolution [H AEC] was used to separate hematoxylin, followed by postprocessing steps for signal cleaning and

BOX 1: ANTIBODIES USED FOR MULTIPLEX IHC

Lymphoid panel:				
	Cycle 1	Cycle 2	Cycle 3	Cycle 4
Target	Round 1	Round 1	Round 1	Round 1
	CC3	PD-1	TCF1/TCF7	CD3
Company/Product	CST (9661S)	CST (84651)	CST (2203S)	Thermo Fisher (RM-9107-S)
Clone	Polyclonal	D7D5W	C63D9	SP7
Dilution	1/100	1/100	1/200	1/300
Duration	RT, 1 hr	ON, 4°C	RT, 1 hr	RT, 1 hr
Secondary species	Rabbit	Rabbit	Rabbit	Rabbit
AEC	1 h 5 min	1 h 20 min	15 min	53 min
Target	Round 2	Round 2	Round 2	
	Hematoxylin	CD45	CD8	
Company/Product	Dako (S330130-2)	BD Bio (550539)	eBioscience (14-0808-82)	
Clone	NA	30-F11	4SM15	
Dilution	Ready to use	1/50	1/100	
Duration	1 min	RT, 1 hr	ON, 4°C	
Secondary species	NA	Rat	Rat	
AEC	NA	52 min	30 min	
Target	Cycle 5	Cycle 6	Cycle 7	Cycle 8
	Round 1	Round 1	Round 1	Round 1
	PD-L1	CD11b	Granzyme B	Ki-67
Company/Product	CST (13684)	Abcam (133357)	Abcam (4059)	Abcam (15580)
Clone	E1L3N	EPR1334	Polyclonal	Polyclonal
Dilution	1/50	1/3,000	1/200	1/1,000
Duration	ON, 4°C	RT, 1 hr	ON	RT, 1 hr
Secondary species	Rabbit	Rabbit	Rabbit	Rabbit
AEC	23 min	17 min	10 min	24 min
Target				Round 2
				panCK
Company/Product				Abcam (ab27988)
Clone				AE1/1E3
Dilution				1/100
Duration				RT, 1 hr
Secondary species				Mouse
AEC				22 min
Target				Round 3
				Hematoxylin
Company/Product				Dako (S330130-2)
Clone				NA
Dilution				Ready to use
Duration				1 min
Secondary species				NA
AEC				NA
Myeloid panel:				
	Cycle 1	Cycle 2	Cycle 3	Cycle 4
Target	Round 1	Round 1	Round 1	Round 1
	F4/80	CSF1R	CD11c	CD206
Company/Product	Serotec	Santa Cruz	CST (97585)	Abcam (64693)
Clone	Cl:A3-1	E2412	D1V9Y	Polyclonal
Dilution	1/200	1/1,000	1/100	1/2,000
Duration	RT, 1 hr	RT, 1 hr	RT, 1 hr	RT, 1 hr
Secondary species	Rat	Rabbit	Rabbit	Rabbit
AEC	22 min	16 min	15 min	43 min

(continued)

BOX 1: ANTIBODIES USED FOR MULTIPLEX IHC (CONTINUED)

Target	Round 2 CD45	Round 2 MHCII
Company/Product	BD Bio (550539)	eBioscience (eBi14-532)
Clone	30-F11	M5/144.15.2
Dilution	1/100	1/200
Duration	ON, 4°C	ON, 4°C
Secondary species	Rat	Rat
AEC	30 min	63 min

Target	Cycle 5 Round 1 PD-L1	Cycle 6 Round 1 Ki-67	Cycle 7 Round 1 CD11b
Company/Product	CST (13684)	Abcam (15580)	Abcam (133357)
Clone	E1L3N	Polyclonal	EPRI1334
Dilution	1/50	1/1,000	1/6,000
Duration	RT, 1 hr	RT, 1 hr	RT, 1 hr
Secondary species	Rabbit	Rabbit	Rabbit
AEC	23 min	24 min	8 min

Target	Round 2 Ly6G	Round 2 panCK	Round 2 Hematoxylin
Company/Product	eBioscience (551459)	Abcam (ab27988)	Dako (S330130-2)
Clone	1A8	AE1/1E3	NA
Dilution	1/200	1/100	Ready to use
Duration	ON, 4°C	RT, 1 hr	1 min
Secondary species	Rat	Mouse	NA
AEC	6 min	22 min	NA

Abbreviations: BD Bio, BD Biosciences; CST, Cell Signaling Technology; NA, not applicable; ON, overnight; RT, room temperature.

background elimination. AEC signal was extracted in FIJI using the NIH plugin RGB_to_CMYK. Color-deconvoluted images were processed in CellProfiler to quantify single-cell mean intensity signal measurements for every stained marker. CellProfiler outputs were loaded into FCS Express 7 Image Cytometry RUO (De Novo Software) software, and hierarchical gating was carried out to classify immune cell populations.

Proliferation Assays

PDAC cells were seeded into 96-well plates at 2×10^3 cells per well in DMEM containing 10% FBS. Cells were treated as indicated in the text with 100 nmol/L GW501516 (Cayman Chemical 10004272) at the time of cell seeding or 5 mg/mL doxycycline (Sigma-Aldrich D9891) 48 hours prior to cell seeding. GW501516 and doxycycline treatments were both replenished every 48 hours for extended time points. After 72 hours or at the time points indicated in the text, cells were lysed with the CellTiter-Glo Luminescent Cell Viability Assay reagent (Promega), and luminescence was read using a GloMax plate reader.

ChIP

ChIP was performed as described previously (55). Briefly, PDAC cells were fixed in 1% formaldehyde, and nuclei were isolated and lysed in buffer containing 1% SDS, 10 mmol/L EDTA, 50 mmol/L Tris-HCl pH 8.0, and protease inhibitors and sheared with a Diagenode Bioruptor to chromatin fragment sizes of 200 to 1,000 base pairs. Chromatin was immunoprecipitated with antibodies to PPAR δ (Abcam ab178866) or acetylated histone H3K9 (Cell Signaling Technology 9649). PPAR δ binding or histone acetylation at known PPAR δ target gene promoter regions was assessed by ChIP-qPCR, and enrichment values were normalized to a control intergenic region of the genome.

The following primer sequences were used: Intergenic F: tgggtctcttg-gtcaatca, R: aggacaaaacagcaaccaaca, *Angptl4* F: tcagcctaccagggagagaa, R: ggaggaaagggcgtacaaa, *Reg3 g* F: actgcaccatacctgacaa, R: ccctag-gatggtgtgtcagg, *Ptgs2* F: gttcttgccgaactcactga, R: agtctgagttcctctcgtga, *Csf1* F: gaaggctgctcatccattg, R: gggcctaataaacatgtgcaa, and *Cxcl2* F: gcttgaacacacacacacct, R: ctatgggacctgggatgtc.

Gene Expression Analysis by qPCR

The isolated total RNA (1 μ g) was reverse-transcribed to produce cDNA using the iScript Reverse Transcription Supermix kit (Bio-Rad). Real-time PCR was performed using SYBR Green supermix (Bio-Rad). The cDNA sequences for specific gene targets were obtained from the human genome assembly (<http://genome.ucsc.edu>), and gene-specific primer pairs were designed using the Primer3 program (<https://primer3.ut.ee/>). Relative gene expression was normalized using the 36B4 housekeeping gene. The following primer sequences were used: human and mouse 36B4 (*RPLP0*): F: 5'-GTGCT GATGGGCAAGAAC-3'; R: 5'-AGGTCCTCCTTGGTGAAC-3'; mouse *Ptgs2*: F: 5'-TGAGTGGGGTGATGAGCAAC-3'; R: 5'-TTCAGAGGCAAT GCGGTTCT-3'; mouse *Pdk4*: F: 5'-TGAACATCCTTCGGTGCAG-3'; R: 5'-GTCCACTGTGACAGGTGTCTT-3'; mouse *Csf1*: F: 5'-ATGAG CAGGAGTATTGCCAAGG-3'; R: 5'-TCCATTCCAATCATGTGGCTA-3'; and mouse *Reg3g*: F: 5'-ATGCTTCCCCGTATAACCATCA-3'; R: 5'-GGCCATATCTGCATCATACCAG-3'.

Analysis of GOT2 Expression and PPAR δ Activity in TCGA-PAAD

To assess the correlation between *GOT2* and PPAR δ activity in a larger compendium of human PDAC samples, we downloaded the

pancreatic cancer RNA-seq fragments per kilobase million gene expression data from TCGA-PAAD using the Bioconductor (56) R package (version 2.15.3). We built the PPAR δ target gene signature using the PPAR δ -regulated genes defined in a previous study (40). Then, we used the gene set variation analysis (GSVA) algorithm (57) with the default settings, as implemented in the GSVA R package (version 1.34.0), to calculate the enrichment of PPAR δ target genes as PPAR δ activity score for each sample and plotted this against *GOT2* expression.

Metascape Analysis

The PDAC TCGA Firehose Legacy database provides mRNA expression data for coexpression analysis accessible through cBioPortal. The data set includes Spearman correlation analysis and *P* values for each gene comparison. The data set was used to identify genes negatively or positively correlated with *GOT2* expression in patients with PDAC. A list of genes with a Spearman correlation value of equal to or less than -0.25 (negative correlation) or equal to or greater than 0.25 (positive correlation) and a *P* value of less than 0.01 was generated. The list of genes was submitted to the online bioinformatics tool Metascape for the identification of enriched gene ontology clusters in the data set. The output from the Metascape analysis was graphed using GraphPad Prism.

Cytokine Array

Control and sgGOT2 FC1245 cells were respectively seeded into a 6-well plate at 5×10^5 cells per well in growth medium (DMEM with 10% FBS and 1% penicillin and streptomycin). The next day, the growth medium was removed and replaced with 1 mL of serum-free DMEM. The supernatant was collected 48 hours after media change and spun down at $1,500 \times g$ for 10 minutes before proceeding to cytokine array using the Proteome Profiler Mouse XL Cytokine Array Kit (R&D ARY028). The assay was completed as per the manufacturer's instructions. Membranes were blocked for 1 hour at room temperature using Array Buffer 6, followed by overnight incubation of supernatant samples at 4°C . After overnight incubation, blots were washed three times for 10 minutes per wash using $1\times$ wash buffer. Diluted detection antibody cocktail (1.5 mL) was then added to the membranes and incubated for 1 hour on a shaker at room temperature. Wash steps were repeated similarly to prior wash steps. Membranes were then incubated with 2 mL of diluted IRDye 800CW Streptavidin (Li-COR Biosciences 926-32230) on a shaking platform for 30 minutes at room temperature. Wash steps were repeated after streptavidin incubation, and membranes were read using the Odyssey CLx infrared imaging system (Li-COR Biosciences).

Orthotopic PDAC Modeling

The orthotopic transplant method used here was described previously (58). In brief, 8- to 10-week-old, wild-type male C57BL/6J (for FC1245) or B6129SF1/J (for 688M) mice were orthotopically transplanted as described previously with 5×10^3 FC1245 cells or 8×10^4 688M cells in 50% Matrigel (Corning 356231) and 50% DMEM. For experiments with 688M cells harboring VP16-PPAR δ , 6×10^4 688M cells were used. For pharmacologic activation of PPAR δ , mice were treated with vehicle (5% PEG-400, 5% Tween-80 in diH₂O) or with 4 mg/kg GW501516 in vehicle by i.p. injection once daily. Vehicle was created and autoclaved before use. GW501516 was created in 10 mmol/L stock in DMSO and stored in 250 μL aliquots at -20°C (one for each day of treatment). On the day of treatment, a vial was thawed and diluted 1:10 in vehicle, and mice were dosed at 4 mg/kg. For T-cell depletion experiments, mice received an i.p. injection of 0.2 mg of αCD8 (2.43), αCD4 (GK1.5), or an IgG2b isotype control (LTF-2) diluted in 100 μL sterile PBS. Antibodies were purchased from Bio X Cell and were administered beginning 2 days preimplantation with 6×10^4 688M cells and every 4 days thereafter until euthanasia, as previously described (23). Mice were euthanized when control animals were moribund, and tumors were excised, weighed, and immediately fixed in formalin.

Long-Chain Fatty Acid Binding Site Prediction

The arachidonic acid binding site on the human GOT2 surface is predicted using the molecular modeling technique. Druggable hotspot identification has long been used to predict and explore the allosteric pockets that accommodate substrate and drug-like molecules (59, 60). A similar approach was taken to identify a plausible arachidonic acid binding site by probing the GOT2 3D protein structure (ref. 36; PDBID:5AX8). The protein structure was prepared using the protein prep tool of Maestro-2014-3 (Schrödinger, LLC). Arachidonic acid is a 20-carbon long-chain fatty acid (LCFA) with greasy carbons and a carboxylate group. The available structural information suggests that the binding pocket must be hydrophobic with the positively charged residues to accommodate LCFA (61, 62).

The SiteMap (63) calculation accounts for the prediction of pockets, characterized by cavity volume, chemical, and physical properties as that of known druggable sites. Five sites were predicted on the GOT2 structure, and these sites had a site score of >0.8 , composed of hydrophobic, hydrogen bond acceptor, and donor volumes. The top-ranked site 1 is a catalytic site, and sites 2 to 5 are allosteric. Arachidonic acid docked against all the predicted sites. The Induced-Fit docking protocol (64) adopted here allows both the ligand and the surrounding residues of protein to be flexible. A total of five docking runs were performed on the predicted site. The docking grid boxes were defined based on the residues suggested by the SiteMap analysis (site 1: N215, H210; site 2: N270, F239; site 3: A260, W226, H373, G385, Q390; site 4: R337, G254; site 5: N332, D93). The site 2 ~ 25 Å away from the catalytic site resulted in a binding pose with favorable energy and interaction complementarity between the protein and ligand. Compared with other sites, site 2 has increased hydrophobic volume, which may recognize LCFA-like arachidonic acid. Triple mutants K234A/K296/R303 were proposed to validate the predicted binding pose. K234 interacts with the carboxylate group of LCFA. K296, which is in proximity to making ionic interaction (in dynamics) and perturbation of the positive charge to neutral alanine residues, prevents the charged interaction. From the docking pose, R303 is making the hydrophobic interaction with the lipid tail of arachidonic acid. R303A mutation reduces the hydrophobic interaction by the side chain of arginine. The proposed triple mutations have the potential to abolish the arachidonic acid binding.

Fatty Acid Binding Assay

Reactions were carried out in binding buffer (0.003% digitonin in $1\times$ PBS) containing 1 $\mu\text{mol/L}$ of purified human GOT2 protein (AA30-430) and 0.5 $\mu\text{Ci/mL}$ [^3H]-arachidonic acid. After incubation for 1 hour at 4°C , the mixture was incubated with preequilibrated TALON Metal Affinity Resin (Takara, 635502) at 4°C for 1 hour and loaded onto a column and washed with binding buffer, then binding buffer with 0.01% BSA, and then binding buffer again. The protein-bound [^3H]-arachidonic acid was eluted with elution buffer (50 mmol/L sodium phosphate, 300 mmol/L sodium chloride, 150 mmol/L imidazole; pH 7.4.) and quantified by scintillation counting. For competition experiments with unlabeled lipids, the assays were carried out in the presence of ethanol containing the indicated unlabeled sterol (0–1 mmol/L).

Luciferase Assay

The PPRE x3-TK-Luc (PPAR response element driving luciferase) plasmid #1015 was purchased from Addgene, and the Renilla plasmid (pRL-SV40) was generously provided by Dr. Ellen Langer (OHSU). Cells were transfected with 2.5 μg PPRE x3-TK-Luc, 15 ng pRL-SV40, and 4 μL Lipofectamine 2000 in 6-well plates. Briefly, cells were plated at 1×10^6 per well of a 6-well plate and allowed to adhere overnight. Plasmids were combined in 150 μL Opti-MEM, whereas Lipofectamine 2000 was combined in a separate tube with 150 μL Opti-MEM. After 5 minutes, the tubes were combined. The mixture (300 μL) was added, in a dropwise manner, to 700 μL of Opti-MEM

on each well for transfection. The cells were incubated overnight at 37°C, collected, counted, and replated to white-walled, 96-well plates in triplicates. Twenty-four hours later, a dual-luciferase assay was completed following the manufacturer's instructions: Dual-Luciferase Reporter Assay System (Promega E1910). Briefly, cells were lysed in white-walled, 96-well plates with 20 μ L 1 \times Passive Lysis Buffer and shaken on a room temperature shaker. LARII (100 μ L) was added to each well, and luminescence was measured over 5 seconds. Stop and Glo (100 μ L) was then added, and Renilla activity was measured with luminescence over 5 seconds. Activity was calculated by normalizing the luciferase signal to Renilla for each well.

PPAR δ Transcription Factor Activity Assay

Nuclear lysates were prepared using a detergent-free fractionation protocol. Cells were scraped and collected from 10-cm dishes, washed with PBS, pelleted (450 \times g 5 minutes), resuspended in PBS, and 1/5 of the volume was reserved for whole-cell lysis in RIPA (Amresco N653-100 mL) + cOmplete EDTA-free protease inhibitor cocktail (Sigma-Aldrich 11836170001). The remaining 4/5 of cell suspension was centrifuged (450 \times g 5 minutes), PBS was removed, and cells were lysed on ice for 15 minutes in lysis buffer (5 \times of cell pellet volume). Lysis buffer consisted of 10 mmol/L HEPES pH 7.9, 1.5 mmol/L MgCl₂, and 10 mmol/L KCl with 1 mmol/L DTT and EDTA-Free cOmplete mini protease inhibitor cocktail. Lysates were centrifuged (450 \times g 5 minutes), supernatant was decanted, lysis buffer was added (2 \times cell volume), and suspensions were ground on ice with a plastic homogenizer 10 \times in 1.5 mL Eppendorf tubes. Lysates were centrifuged (10,000 \times g 20 minutes), and supernatant was collected as a cytosolic fraction. The remaining pellet was washed with 200 μ L lysis buffer (10,000 \times g 5 minutes), the supernatant was decanted, and extraction buffer was added (2/3 \times cell pellet volume). Extraction buffer consisted of 20 mmol/L HEPES pH 7.9, 1.5 mmol/L MgCl₂, 0.42M NaCl, 0.2 μ mol/L EDTA, 25% glycerol (V/V), and 1 mmol/L DTT and cOmplete mini EDTA-free protease inhibitor cocktail. Nuclei were ground with a plastic homogenizer in 1.5 mL Eppendorf tubes 20 \times and incubated at 4°C with gentle shaking for 10 minutes. Samples were centrifuged (20,000 \times g 5 minutes), and the supernatant was transferred to cold Eppendorf tubes as a nuclear fraction. Lysates were measured with BCA, and an equal protein amount was added per sample for each well. The manufacturer's instructions were followed for the PPAR δ transcription factor kit (Abcam ab133106). Briefly, CTFB was prepared and added to blank and nonspecific binding wells, nuclear lysates were added to each sample well containing immobilized PPRE-containing DNA, and the plate was incubated overnight at 4°C without agitation. The next day, wells were washed 5 \times in 1 \times wash buffer and incubated in PPAR δ primary antibody (1:100) for 1 hour at room temperature in the dark, without agitation. Wells were washed 5 \times in 1 \times wash buffer and incubated in goat anti-rabbit HRP conjugate (1:100) for 1 hour at room temperature in the dark without agitation. Wells were washed 5 \times in 1 \times wash buffer, and 100 μ L developing solution was added to each well. The plate was incubated for 15 to 45 minutes on a room temperature shaker, in the dark, until color developed. Stop solution (100 μ L) was added to the wells, and the absorbance at 450 nm was taken.

RNA-seq

Control or sgGot2 FC1245 PDAC cells were untreated or treated with 500 nmol/L GW501516 for 24 hours, and RNA was isolated by TRIzol extraction per the manufacturer's instructions and cleaned up using an RNeasy kit (Qiagen). Treatments were performed in triplicate. RNA-seq libraries were prepared using the Illumina TruSeq Stranded mRNA kit using 300-ng total RNA as input and 15 rounds of amplification. Libraries were sequenced on an Illumina NextSeq 500 (~30 million reads per sample). The quality of the raw sequencing files was evaluated using FastQC (<https://www.bioinformatics.babraham.ac.uk/projects/>

fastqc/) combined with MultiQC (ref. 65; <http://multiqc.info/>). Trimmomatic (66) was used to remove any remaining Illumina adapters. Reads were aligned to Ensembl's GRCm38 along with its corresponding annotation, release 104. The program STAR (ref. 67; v2.7.3a) was used to align the reads to the genome. STAR has been shown to perform well compared with other RNA-seq aligners (68). Since STAR utilizes the gene annotation file, it also calculated the number of reads aligned to each gene. RNA-SeQC (69) and another round of MultiQC were utilized to ensure alignments were of sufficient quality. Gene-level differential expression analysis was performed in open source software R (R Core Team). Gene-level raw counts were filtered to remove genes with extremely low counts in many samples following the published guidelines (70), normalized using the trimmed mean of M-values (71), and transformed to log-counts per million with associated observational precision weights using the voom (72) method. Gene-wise linear models for control versus knocked out for Got2 (sgGot2) were used for differential expression analyses using limma with empirical Bayes moderation (73) and false discovery rate adjustment. Gene set enrichment analysis using fgsea was used to compare differentially expressed genes from control and sgGot2 PDAC cells to PPAR δ target genes defined in a previous study (40). Gene ontology and pathway analyses were performed using Ingenuity Pathway Analysis or Enrichr. Two-way comparison (control versus sgGot2) and four-way comparison (control versus sgGot2 \pm GW501516) were performed with independent sgGot2 clones.

Nuclear Fatty Acid Uptake Assay

MIA PaCa-2 ctrl and sh27 cells were plated at 5 \times 10⁵ in a 6-well plate and allowed to adhere overnight. The media were changed to 0% FBS DMEM, and the cells were incubated for 24 hours. The media was changed to 0.5% fatty acid-free BSA DMEM with either chloroform (ctrl) or 2.5 μ mol/L NBD-arachidonic acid (Avanti Polar Lipids 810106C). Media were made before being added to cells, heated to 37°C, and vortexed until fatty acid was completely in solution. Cells were incubated at 37°C for durations indicated in the manuscript and collected and fractionated using the detergent-free method described above (PPAR δ transcription factor activity assay). Nuclear lysates were placed in a white-walled, 96-well plate, and fluorescence was measured at 480 nm excitation and 540 nm emission. Lysate concentration was measured using a BCA kit. FC1245 cells were plated at 5 \times 10⁵ per well and treated as described above, but treatment was reduced to 2 μ mol/L NBD-arachidonic acid for 15 minutes due to lipid toxicity in this cell line.

Aspartate Aminotransferase Assay

The AST Activity Assay Kit (Sigma-Aldrich MAK055) was used to determine aspartate aminotransferase activity per the manufacturer's instructions. Briefly, this assay determines the transfer of an amino group from aspartate to alpha-ketoglutarate in the generation of glutamate, which produces a colorimetric product (450 nm) that is proportional to aspartate aminotransferase activity in the sample. For this assay, PA-TU-8988T cells with stable expression of doxycycline-inducible GOT2 shRNA were transiently transfected with wtGOT2 and tmGOT2. After 48 hours, these cells were exposed to doxycycline for 48 hours to knock down endogenous GOT2 in cells with GOT2 shRNA. Cells were seeded at 5 \times 10⁶ and collected via trypsin dissociation after cells were adhered. The cells were then resuspended in 1 mL of ice-cold 1 \times PBS and 200 μ L (1 \times 10⁶ cells) and were collected for the AST assay, and 800 μ L (4 \times 10⁶ cells) were collected for protein concentration estimation and Western blot protein expression analysis. Using AST assay kit buffers, cells were lysed to obtain a supernatant that was combined with the kit reagent master mix to detect glutamate in a colorimetric reaction. The samples were read every 5 minutes for 30 minutes. AST activity and concentration in the samples were determined using instructions from the manufacturer.

Free Fatty Acid Measurements

Samples were subjected to an LC-MS analysis to detect and quantify levels of free fatty acids in sample extracts. A fatty acid extraction was carried out on each sample using 100% methanol as the homogenization solvent. Whole-cell pellets (1×10^6 cells/sample) were lysed with 1,000 μ L of methanol and ~ 100 μ L of zircon beads (0.5 mm). Manual disruption with a p1000 pipette tip was performed to assist with initial pellet suspension in the extraction buffer. The methanol extracts were centrifuged ($21,000 g \times 3$ minutes) and transferred to glass LC-MS inserts for analysis. The LC column was a WatersTM BEH-C18 (2.1×100 mm, 1.7 μ m) coupled to a Dionex Ultimate 3000 system, and the column oven temperature was set to 25°C for the gradient elution. The flow rate was 0.1 mL/minute and used the following buffers: (A) water with 0.1% formic acid and (B) acetonitrile with 0.1% formic acid. The gradient profile was as follows: 60% to 99% B from 0 to 6 minutes, hold at 99% B from 6 to 10 minutes, 99% to 60% B from 10 to 11 minutes, hold at 60% B from 11 to 15 minutes. Injection volume was set to 1 μ L for all analyses (15 minutes of total run time per injection).

MS analyses were carried out by coupling the LC system to a Thermo Q Exactive HFTM mass spectrometer operating in heated electrospray ionization mode. Data acquisition was 10 minutes with a negative mode full MS scan (profile mode) and one microscan, with an AGC target of $3e6$ and a maximum IT of 100 ms at 120,000 resolution, with a scan range from 160 to 400 m/z. Spray voltage was 3.5 kV, and the capillary temperature was set to 320°C with a sheath gas rate of 35, aux gas of 10, and max spray current of 100 μ A. The acquisition order of samples and standard curve points was randomized, with blank matrix controls before and after each standard curve point to assess carryover (none detected). The resulting free fatty acid peaks were quantified by measuring the relative intensities (peak heights) of the high resolution extracted ion chromatogram (XIC) for each fatty acid across the samples and external standard curve samples ranging from 10 μ g/mL to 100 ng/mL. All fatty acids were detected as the negative mode [M-H] ion, and retention times of the fatty acids were defined using a cocktail of authentic standards. For each XIC, the theoretical m/z of each fatty acid (± 5 ppm) was used to extract the peak height (24 seconds retention time window, 12 seconds retention time tolerance) as follows: lauric acid (199.1704 m/z, 2.3 minutes), myristic acid (227.2017 m/z, 3.1 minutes), palmitoleic acid (253.2173 m/z, 3.4 minutes), palmitic acid (255.2330 m/z, 4.1 minutes), oleic acid (281.2486 m/z, 4.4 minutes), stearic acid (283.2643 m/z, 5.1 minutes), arachidic acid (311.2956 m/z, 6.0 minutes), nervonic acid (365.3425 m/z, 6.9 minutes), and lignoceric acid (367.3582 m/z, 7.5 min). The resulting standard curve points (in duplicate) were fit to a linear regression (GraphPad Prism 8), and this equation was used to interpolate the concentration of fatty acids in the sample extracts, as prepared.

Statistical Analysis

All statistical analyses were performed using GraphPad Prism 9.0 Software (GraphPad Software Inc.).

Data Availability

All sequencing data from this study have been deposited in the Sequence Read Archive under BioProject ID PRJNA782676.

Authors' Disclosures

L.M. Coussens reports personal fees from (P30) Koch Institute for Integrated Cancer Research, Massachusetts Institute of Technology, Bloomberg-Kimmel Institute for Cancer Immunotherapy, Sidney Kimmel Comprehensive Cancer Center at Johns Hopkins, (P50) Dana-Farber Cancer Center Breast SPOR, (P30) Dana-Farber/Harvard Cancer Center, (P30) University of California, San Diego Moores Cancer Center, (P30) The Jackson Laboratory Cancer Center, (P01) Columbia University Medical Center, Prostate P01, (P50) MD Anderson Cancer Center Gastrointestinal SPOR, the Cancer Research Institute, the

Lustgarten Foundation for Pancreatic Cancer Research, the Therapeutics Working Group, the NIH/NCI-Frederick National Laboratory Advisory Committee, AbbVie Inc., Shasqi, Inc., and the American Association for Cancer Research (AACR): *Cancer Immunology Research*, personal fees and nonfinancial support from Cell Signaling Technology, nonfinancial and other support from ZellBio, Inc. and Syndax Pharmaceuticals Inc., personal fees, nonfinancial, and other support from HiberCell, Inc., personal fees and other support from the Susan G. Komen Foundation, and other support from Pharmacyclics, Inc.: steering committee for PCYC-1137-CA, the AACR: *Cancer Discovery*, the AACR, *Cancer Cell*, the Prospect Creek Foundation, the Lustgarten Foundation for Pancreatic Cancer Research, Carisma Therapeutics Inc., CytomX Therapeutics, Inc., Kineta Inc., Alkermes, Inc., PDX Pharmaceuticals, Inc., Zymeworks, Inc., AstraZeneca Partner of Choice Network, Genenta Sciences, and Pio Therapeutics Pty Ltd during the conduct of the study. M.H. Sherman reports personal fees from Autobahn Labs outside the submitted work. No disclosures were reported by the other authors.

Authors' Contributions

J. Abrego: Conceptualization, resources, data curation, formal analysis, validation, investigation, visualization, methodology, writing—original draft, writing—review and editing. **H. Sanford-Crane:** Conceptualization, resources, data curation, formal analysis, funding acquisition, investigation, methodology, writing—review and editing. **C. Oon:** Conceptualization, data curation, formal analysis, validation, investigation, visualization, methodology, writing—review and editing. **X. Xiao:** Data curation, investigation, writing—review and editing. **C.B. Betts:** Conceptualization, data curation, formal analysis, investigation, visualization, methodology, writing—review and editing. **D. Sun:** Data curation, formal analysis, visualization, writing—review and editing. **S. Nagarajan:** Resources, formal analysis, investigation, visualization, methodology, writing—review and editing. **L. Diaz:** Data curation, formal analysis, investigation, writing—review and editing. **H. Sandborg:** Data curation, formal analysis, validation, investigation, writing—review and editing. **S. Bhattacharyya:** Data curation, formal analysis, investigation, visualization, writing—review and editing. **Z. Xia:** Resources, data curation, formal analysis, supervision, investigation, visualization, writing—review and editing. **L.M. Coussens:** Resources, data curation, formal analysis, supervision, investigation, visualization, methodology, writing—review and editing. **P. Tontonoz:** Data curation, formal analysis, supervision, investigation, writing—review and editing. **M.H. Sherman:** Conceptualization, resources, data curation, formal analysis, supervision, funding acquisition, validation, investigation, visualization, methodology, writing—original draft, writing—review and editing.

Acknowledgments

We thank all members of the Sherman lab as well as Drs. Sara Courtneidge, Kimberly Beatty, and Amy Moran for helpful discussion of this work. This study was supported by a postdoctoral fellowship from the OHSU Fellowship for Diversity in Research (to J. Abrego), a graduate student fellowship from the Knight Cancer Institute Cancer Center Support Grant P30 CA069533 (to H. Sanford-Crane), NIH grants R00 CA188259 and R01 CA229580 (to M.H. Sherman) including CA229580-S1 Research Supplement to Promote Diversity in Health-Related Research (awarded to M.H. Sherman in support of J. Abrego), American Cancer Society grant RSG-18-142-01-CSM (to M.H. Sherman), and an OHSU Faculty Innovation Fund Award (to M.H. Sherman). L.M. Coussens acknowledges funding from the NIH (1U01 CA224012, U2C CA233280, R01 CA223150, R01 CA226909, and R21 HD099367), the Knight Cancer Institute, and the Brenden-Colson Center for Pancreatic Care at OHSU. Development of analytical methods used for image analysis at OHSU were developed and carried out with major support from the NIH, the NCI

Human Tumor Atlas Network Research Center (U2C CA233280), and the Prospect Creek Foundation to the OHSU SMMART (Serial Measurement of Molecular and Architectural Responses to Therapy) Program. P. Tontonoz acknowledges funding from the NIH (R01 DK126779). We thank members of the OHSU Histopathology Shared Resource, Medicinal Chemistry Core, Massively Parallel Sequencing Shared Resource, Bioinformatics and Biostatistics Core, KCVI Epigenetics Consortium, and Advanced Light Microscopy Shared Resource for supporting this study, as well as Dr. Drew Jones and Leonard Ash from the NYU Langone Health Metabolomics Laboratory.

The costs of publication of this article were defrayed in part by the payment of page charges. This article must therefore be hereby marked *advertisement* in accordance with 18 U.S.C. Section 1734 solely to indicate this fact.

Note

Supplementary data for this article are available at Cancer Discovery Online (<http://cancerdiscovery.aacrjournals.org/>).

Received June 8, 2022; revised July 10, 2022; accepted July 22, 2022; published first July 27, 2022.

REFERENCES

- van Karnebeek CDM, Ramos RJ, Wen XY, Tarailo-Graovac M, Gleeson JG, Skrypnik C, et al. Bi-allelic GOT2 mutations cause a treatable malate-aspartate shuttle-related encephalopathy. *Am J Hum Genet* 2019;105:534–48.
- Yang H, Zhou L, Shi Q, Zhao Y, Lin H, Zhang M, et al. SIRT3-dependent GOT2 acetylation status affects the malate-aspartate NADH shuttle activity and pancreatic tumor growth. *EMBO J* 2015;34:1110–25.
- Yang S, Hwang S, Kim M, Seo SB, Lee JH, Jeong SM. Mitochondrial glutamine metabolism via GOT2 supports pancreatic cancer growth through senescence inhibition. *Cell Death Dis* 2018;9:35.
- Hollinshead KER, Parker SJ, Eapen VV, Encarnacion-Rosado J, Sohn A, Oncu T, et al. Respiratory supercomplexes promote mitochondrial efficiency and growth in severely hypoxic pancreatic cancer. *Cell Rep* 2020;33:108231.
- Sorrentino D, Stump D, Potter BJ, Robinson RB, White R, Kiang CL, et al. Oleate uptake by cardiac myocytes is carrier mediated and involves a 40-kD plasma membrane fatty acid binding protein similar to that in liver, adipose tissue, and gut. *J Clin Invest* 1988;82:928–35.
- Isola LM, Zhou SL, Kiang CL, Stump DD, Bradbury MW, Berk PD. 3T3 fibroblasts transfected with a cDNA for mitochondrial aspartate aminotransferase express plasma membrane fatty acid-binding protein and saturable fatty acid uptake. *Proc Natl Acad Sci U S A* 1995;92:9866–70.
- Luiken JJ, Turcotte LP, Bonen A. Protein-mediated palmitate uptake and expression of fatty acid transport proteins in heart giant vesicles. *J Lipid Res* 1999;40:1007–16.
- Chabowski A, Coort SL, Calles-Escandon J, Tandon NN, Glatz JF, Luiken JJ, et al. The subcellular compartmentation of fatty acid transporters is regulated differently by insulin and by AICAR. *FEBS Lett* 2005;579:2428–32.
- Bradbury MW, Berk PD. Mitochondrial aspartate aminotransferase: direction of a single protein with two distinct functions to two subcellular sites does not require alternative splicing of the mRNA. *Biochem J* 2000;345:423–7.
- Bradbury MW, Stump D, Guarnieri F, Berk PD. Molecular modeling and functional confirmation of a predicted fatty acid binding site of mitochondrial aspartate aminotransferase. *J Mol Biol* 2011;412:412–22.
- Stremmel W, Strohmeier G, Borchard F, Kochwa S, Berk PD. Isolation and partial characterization of a fatty acid binding protein in rat liver plasma membranes. *Proc Natl Acad Sci U S A* 1985;82:4–8.
- Stump DD, Zhou SL, Berk PD. Comparison of plasma membrane FABP and mitochondrial isoform of aspartate aminotransferase from rat liver. *Am J Physiol* 1993;265:G894–902.
- Stremmel W, Strohmeier G, Berk PD. Hepatocellular uptake of oleate is energy dependent, sodium linked, and inhibited by an antibody to a hepatocyte plasma membrane fatty acid binding protein. *Proc Natl Acad Sci U S A* 1986;83:3584–8.
- Auciello FR, Bulusu V, Oon C, Tait-Mulder J, Berry M, Bhattacharyya S, et al. A stromal lysolipid-autotaxin signaling axis promotes pancreatic tumor progression. *Cancer Discov* 2019;9:617–27.
- Alicea GM, Rebecca VW, Goldman AR, Fane ME, Douglass SM, Behera R, et al. Changes in aged fibroblast lipid metabolism induce age-dependent melanoma cell resistance to targeted therapy via the fatty acid transporter FATP2. *Cancer Discov* 2020;10:1282–95.
- Zou Y, Watters A, Cheng N, Perry CE, Xu K, Alicea GM, et al. Polyunsaturated fatty acids from astrocytes activate PPARgamma signaling in cancer cells to promote brain metastasis. *Cancer Discov* 2019;9:1720–35.
- Zhang M, Di Martino JS, Bowman RL, Campbell NR, Baksh SC, Simon-Vermot T, et al. Adipocyte-derived lipids mediate melanoma progression via FATP proteins. *Cancer Discov* 2018;8:1006–25.
- Pascual G, Avgustinova A, Mejetta S, Martin M, Castellanos A, Attolini CS, et al. Targeting metastasis-initiating cells through the fatty acid receptor CD36. *Nature* 2017;541:41–5.
- Chakrabarti G, Moore ZR, Luo X, Ilcheva M, Ali A, Padanad M, et al. Targeting glutamine metabolism sensitizes pancreatic cancer to PARP-driven metabolic catastrophe induced by β -lapachone. *Cancer Metab* 2015;3:12.
- Mitchem JB, Brennan DJ, Knolhoff BL, Belt BA, Zhu Y, Sanford DE, et al. Targeting tumor-infiltrating macrophages decreases tumor-initiating cells, relieves immunosuppression, and improves chemotherapeutic responses. *Cancer Res* 2013;73:1128–41.
- Zhu Y, Knolhoff BL, Meyer MA, Nywening TM, West BL, Luo J, et al. CSF1/CSF1R blockade reprograms tumor-infiltrating macrophages and improves response to T-cell checkpoint immunotherapy in pancreatic cancer models. *Cancer Res* 2014;74:5057–69.
- Zhang Y, Velez-Delgado A, Mathew E, Li D, Mendez FM, Flannagan K, et al. Myeloid cells are required for PD-1/PD-L1 checkpoint activation and the establishment of an immunosuppressive environment in pancreatic cancer. *Gut* 2017;66:124–36.
- Evans RA, Diamond MS, Rech AJ, Chao T, Richardson MW, Lin JH, et al. Lack of immunoeediting in murine pancreatic cancer reversed with neoantigen. *JCI Insight* 2016;1:e88328.
- Lawrence JW, Kroll DJ, Eacho PI. Ligand-dependent interaction of hepatic fatty acid-binding protein with the nucleus. *J Lipid Res* 2000;41:1390–401.
- Esteves A, Knoll-Gellida A, Canclini L, Silvarrey MC, Andre M, Babin PJ. Fatty acid binding proteins have the potential to channel dietary fatty acids into enterocyte nuclei. *J Lipid Res* 2016;57:219–32.
- Evans RM, Mangelsdorf DJ. Nuclear receptors, RXR, and the big bang. *Cell* 2014;157:255–66.
- Maniati E, Bossard M, Cook N, Candido JB, Emami-Shahri N, Nedospasov SA, et al. Crosstalk between the canonical NF-kappaB and Notch signaling pathways inhibits Ppargamma expression and promotes pancreatic cancer progression in mice. *J Clin Invest* 2011;121:4685–99.
- Luo Y, Yang Y, Liu M, Wang D, Wang F, Bi Y, et al. Oncogenic KRAS reduces expression of FGF21 in acinar cells to promote pancreatic tumorigenesis in mice on a high-fat diet. *Gastroenterology* 2019;157:1413–28.
- Yuan H, Lu J, Xiao J, Upadhyay G, Umans R, Kallakury B, et al. PPARdelta induces estrogen receptor-positive mammary neoplasia through an inflammatory and metabolic phenotype linked to mTOR activation. *Cancer Res* 2013;73:4349–61.
- Beyaz S, Mana MD, Roper J, Kedrin D, Saadatpour A, Hong SJ, et al. High-fat diet enhances stemness and tumorigenicity of intestinal progenitors. *Nature* 2016;531:53–8.
- Wang D, Fu L, Ning W, Guo L, Sun X, Dey SK, et al. Peroxisome proliferator-activated receptor delta promotes colonic inflammation and tumor growth. *Proc Natl Acad Sci U S A* 2014;111:7084–9.
- Pollock CB, Rodriguez O, Martin PL, Albanese C, Li X, Kopelovich L, et al. Induction of metastatic gastric cancer by peroxisome proliferator-activated receptor delta activation. *PPAR Res* 2010;2010:571783.
- Adhikary T, Kaddatz K, Finkernagel F, Schonbauer A, Meissner W, Scharfe M, et al. Genomewide analyses define different modes of

- transcriptional regulation by peroxisome proliferator-activated receptor-beta/delta (PPARbeta/delta). *PLoS One* 2011;6:e16344.
34. Markosyan N, Li J, Sun YH, Richman LP, Lin JH, Yan F, et al. Tumor cell-intrinsic EPHA2 suppresses anti-tumor immunity by regulating PTGS2 (COX-2). *J Clin Invest* 2019;129:3594–609.
 35. Zelenay S, van der Veen AG, Bottcher JP, Snelgrove KJ, Rogers N, Acton SE, et al. Cyclooxygenase-dependent tumor growth through evasion of immunity. *Cell* 2015;162:1257–70.
 36. Jiang X, Wang J, Chang H, Zhou Y. Recombinant expression, purification and crystallographic studies of the mature form of human mitochondrial aspartate aminotransferase. *Biosci Trends* 2016;10:79–84.
 37. Muralikumar S, Vetrivel U, Narayanasamy A, Das UN. Probing the intermolecular interactions of PPARgamma-LBD with polyunsaturated fatty acids and their anti-inflammatory metabolites to infer most potential binding moieties. *Lipids Health Dis* 2017;16:17.
 38. Wise DR, DeBerardinis RJ, Mancuso A, Sayed N, Zhang XY, Pfeiffer HK, et al. Myc regulates a transcriptional program that stimulates mitochondrial glutaminolysis and leads to glutamine addiction. *Proc Natl Acad Sci U S A* 2008;105:18782–7.
 39. Narkar VA, Downes M, Yu RT, Emblar E, Wang YX, Banayo E, et al. AMPK and PPARdelta agonists are exercise mimetics. *Cell* 2008;134:405–15.
 40. Adhikary T, Wortmann A, Schumann T, Finkernagel F, Lieber S, Roth K, et al. The transcriptional PPARbeta/delta network in human macrophages defines a unique agonist-induced activation state. *Nucleic Acids Res* 2015;43:5033–51.
 41. Steele NG, Carpenter ES, Kemp SB, Sirihorachai VR, The S, Delrosario L, et al. Multimodal mapping of the tumor and peripheral blood immune landscape in human pancreatic cancer. *Nat Cancer* 2020;1:1097–112.
 42. Hegde S, Krisnawan VE, Herzog BH, Zuo C, Breden MA, Knolhoff BL, et al. Dendritic cell paucity leads to dysfunctional immune surveillance in pancreatic cancer. *Cancer Cell* 2020;37:289–307.
 43. Liu Y, Deguchi Y, Wei D, Liu F, Moussalli MJ, Deguchi E, et al. Rapid acceleration of KRAS-mutant pancreatic carcinogenesis via remodeling of tumor immune microenvironment by PPARdelta. *Nat Commun* 2022;13:2665.
 44. Qi L, Martin-Sandoval MS, Merchant S, Gu W, Eckhardt M, Mathews TP, et al. Aspartate availability limits hematopoietic stem cell function during hematopoietic regeneration. *Cell Stem Cell* 2021;28:1982–99.
 45. Hickman TL, Choi E, Whiteman KR, Muralidharan S, Pai T, Johnson T, et al. BOXR1030, an anti-GPC3 CAR with exogenous GOT2 expression, shows enhanced T cell metabolism and improved anti-cell line derived tumor xenograft activity. *PLoS One* 2022;17:e0266980.
 46. Zhang Y, Crawford HC, Pasca di Magliano M. Epithelial-stromal interactions in pancreatic cancer. *Annu Rev Physiol* 2019;81:211–33.
 47. Engle DD, Tiriach H, Rivera KD, Pommier A, Whalen S, Oni TE, et al. The glycan CA19-9 promotes pancreatitis and pancreatic cancer in mice. *Science* 2019;364:1156–62.
 48. Gruner BM, Schulze CJ, Yang D, Ogasawara D, Dix MM, Rogers ZN, et al. An in vivo multiplexed small-molecule screening platform. *Nat Methods* 2016;13:883–9.
 49. Farrell AS, Joly MM, Allen-Petersen BL, Worth PJ, Lanciault C, Sauer D, et al. MYC regulates ductal-neuroendocrine lineage plasticity in pancreatic ductal adenocarcinoma associated with poor outcome and chemoresistance. *Nat Commun* 2017;8:1728.
 50. Son J, Lyssiotis CA, Ying H, Wang X, Hua S, Ligorio M, et al. Glutamine supports pancreatic cancer growth through a KRAS-regulated metabolic pathway. *Nature* 2013;496:101–5.
 51. Tsujikawa T, Kumar S, Borkar RN, Azimi V, Thibault G, Chang YH, et al. Quantitative multiplex immunohistochemistry reveals myeloid-inflamed tumor-immune complexity associated with poor prognosis. *Cell Rep* 2017;19:203–17.
 52. Banik G, Betts CB, Liudahl SM, Sivagnanam S, Kawashima R, Cotecchini T, et al. High-dimensional multiplexed immunohistochemical characterization of immune contexture in human cancers. *Methods Enzymol* 2020;635:1–20.
 53. Schindelin J, Arganda-Carreras I, Frise E, Kaynig V, Longair M, Pietzsch T, et al. Fiji: an open-source platform for biological-image analysis. *Nat Methods* 2012;9:676–82.
 54. Carpenter AE, Jones TR, Lamprecht MR, Clarke C, Kang IH, Friman O, et al. CellProfiler: image analysis software for identifying and quantifying cell phenotypes. *Genome Biol* 2006;7:R100.
 55. Sherman MH, Yu RT, Engle DD, Ding N, Atkins AR, Tiriach H, et al. Vitamin D receptor-mediated stromal reprogramming suppresses pancreatitis and enhances pancreatic cancer therapy. *Cell* 2014;159:80–93.
 56. Colaprico A, Silva TC, Olsen C, Garofano L, Cava C, Garolini D, et al. TCGAAbiolinks: an R/Bioconductor package for integrative analysis of TCGA data. *Nucleic Acids Res* 2016;44:e71.
 57. Hanzelmann S, Castelo R, Guinney J. GSEA: gene set variation analysis for microarray and RNA-seq data. *BMC Bioinf* 2013;14:7.
 58. Collisson EA, Trejo CL, Silva JM, Gu S, Korkola JE, Heiser LM, et al. A central role for RAF→MEK→ERK signaling in the genesis of pancreatic ductal adenocarcinoma. *Cancer Discov* 2012;2:685–93.
 59. Ma B, Nussinov R. Druggable orthosteric and allosteric hot spots to target protein-protein interactions. *Curr Pharm Des* 2014;20:1293–301.
 60. Buhman G, O'Connor C, Zerbe B, Kearney BM, Napoleon R, Kovrigina EA, et al. Analysis of binding site hot spots on the surface of Ras GTPase. *J Mol Biol* 2011;413:773–89.
 61. Nojima S, Fujita Y, Kimura KT, Nomura N, Suno R, Morimoto K, et al. Cryo-EM structure of the prostaglandin E receptor EP4 coupled to G protein. *Structure* 2020;29:252–60.
 62. Matthews S, Belcher JD, Tee KL, Girvan HM, McLean KJ, Rigby SE, et al. Catalytic determinants of alkene production by the cytochrome P450 peroxxygenase OleTJE. *J Biol Chem* 2017;292:5128–43.
 63. Halgren TA. Identifying and characterizing binding sites and assessing druggability. *J Chem Inf Model* 2009;49:377–89.
 64. Sherman W, Day T, Jacobson MP, Friesner RA, Farid R. Novel procedure for modeling ligand/receptor induced fit effects. *J Med Chem* 2006;49:534–53.
 65. Ewels P, Magnusson M, Lundin S, Kaller M. MultiQC: summarize analysis results for multiple tools and samples in a single report. *Bioinformatics* 2016;32:3047–8.
 66. Bolger AM, Lohse M, Usadel B. Trimmomatic: a flexible trimmer for Illumina sequence data. *Bioinformatics* 2014;30:2114–20.
 67. Dobin A, Davis CA, Schlesinger F, Drenkow J, Zaleski C, Jha S, et al. STAR: ultrafast universal RNA-seq aligner. *Bioinformatics* 2013;29:15–21.
 68. Engstrom PG, Steijger T, Sipos B, Grant GR, Kahles A, Ratsch G, et al. Systematic evaluation of spliced alignment programs for RNA-seq data. *Nat Methods* 2013;10:1185–91.
 69. DeLuca DS, Levin JZ, Sivachenko A, Fennell T, Nazaire MD, Williams C, et al. RNA-SeQC: RNA-seq metrics for quality control and process optimization. *Bioinformatics* 2012;28:1530–2.
 70. Chen Y, Lun AT, Smyth GK. From reads to genes to pathways: differential expression analysis of RNA-Seq experiments using Rsubread and the edgeR quasi-likelihood pipeline. *F1000Res* 2016;5:1438.
 71. Robinson MD, Oshlack A. A scaling normalization method for differential expression analysis of RNA-seq data. *Genome Biol* 2010;11:R25.
 72. Law CW, Chen Y, Shi W, Smyth GK. voom: precision weights unlock linear model analysis tools for RNA-seq read counts. *Genome Biol* 2014;15:R29.
 73. Ritchie ME, Phipson B, Wu D, Hu Y, Law CW, Shi W, et al. limma powers differential expression analyses for RNA-sequencing and microarray studies. *Nucleic Acids Res* 2015;43:e47.